

Turbulent shear layers in a uniformly stratified background: DNS at high Reynolds number

Alexandra VanDine¹, Hieu T. Pham¹ and Sutanu Sarkar^{1,2+};

¹Department of Mechanical and Aerospace Engineering, University of California, San Diego, La Jolla, CA 92093, USA

²Scripps Institution of Oceanography, University of California San Diego, La Jolla, CA 92093, USA

(Received 20 July 2020; revised 22 January 2021; accepted 1 March 2021)

Direct numerical simulations are performed to investigate a stratified shear layer at high Reynolds number (Re) in a study where the Richardson number (Ri) is varied among cases. Unlike previous work on a two-layer configuration in which the shear layer resides between two layers with constant density, an unbounded fluid with uniform stratification is considered here. The evolution of the shear layer includes a primary Kelvin-Helmholtz shear instability followed by a wide range of secondary shear and convective instabilities, similar to the two-layer configuration. During transition to turbulence, the shear layers at low Ri exhibit a period of thickness contraction (not observed at lower Re) when the momentum and buoyancy fluxes are counter-gradient. The behaviour in the turbulent regime is significant integred with a two-layer density profile. The transition layers, which are zones with elevated shear and stratification that form at the shear-layer edges, are stronger and also able to support a significant internal wave flux. After the shear layer becomes turbulent, mixing in the transition layers, is shown to be more efficient than that which develops in the centre of the shear layer. Overall, the cumulative mixing efficiency (E.C.) is larger than the often assumed value of 1/6. Also, E^{c.} is found to be smaller than that in the two-layer configuration at moderate Ri. It is relatively less sensitive to background stratification, exhibiting little variation for 0.08 & Ri & 5.0.2. The dependence of mixing efficiency on buoyancy Reynolds number during the turbulence phase is

Inhibit shear instabilities and shear-driven turbulence. Quantifying the rate of mixing has important implications in large-scale ocean and atmospheric models. Field observations and general circulation models rely heavily on the parametrization of mixing efficiency (E) to quantify or prescribe the effect of turbulence, where E is understood to be the ratio of the gain in the background potential energy over the sum of the gain plus the dissipation rate of turbulent kinetic energy. For example, some ocean observations use E to estimate turbulent diffusivity (K_O) and thereby vertical heat flux, while ocean models use E for subgrid turbulence closure (Jayne 2009) Whalen et al. 2015, Gregg et al. 2018). An accurate description of E is key in data interpretation and model prediction and the present study aims to improve our existing understanding of the mixing processes in stratified shear flows in nature and engineering.

One popular model is that suggested in Osborn (1980) in which the turbulent diffusivity is simply parameterized as $K_O = \Gamma K_R E_D$, where κ is the molecular diffusivity, $\Gamma = E/(1-E)$ is the flux coefficient (similar to the flux Richardson number) and $Re_D = x/\nu N^2$ is the buoyancy Reynolds number defined using the turbulent dissipation rate (s) and the squared buoyancy frequency (N^2) . Here, Osborn's formula is interpreted in the context of irreversible mixing (twy & Imberger 1991; Venayagamontry & Koseff 2016). Osborn (1980) suggested an upper-bound value of 0.2 for Γ . The validity of Osborn's model and, more specifically, the question of whether Γ has a fixed value, have received much attention. It has been shown that the flux coefficient Γ varies with Prandful number (Pr), buoyancy Reynolds number, turbulent Froude number (Pr) are swith Prandful number (Pr), buoyancy Reynolds number, turbulent Froude number (Pr) and (Pr) where (Pr) is the proposed three regimes of mixing: a diffusive regime in which (Pr) for (Pr) is (Pr) for (Pr) in contrast, Portwood, de

Turbulent shear layers in a uniformly stratified background

ligher value than 0.2, (2) \(\int \) peaks at an intermediate value of stratification where secondary shear instabilities are the richest, and (3) the value of \(\int \) varies significantly with Reynolds number, Prandtl number, Richardson number and even the amount of pre-existing turbulence in the shear layer (Brucker & Sarkar 2007; Kaminski & Smyth 2019).

Nearly all DNS of stratified layers at high Reynolds numbers use a hyperbolic tangent profile for both velocity and density in order to represent a shear layer that develops between two layers having different but constant density. In the oceans and atmosphere, it is typical that the stratification extends beyond the region of shear such that a spatially extensive stratification is a more appropriate representation of the density gradient than the spatially compact stratification of the two-layer profile. We are therefore motivated to simulate the evolution of a shear layer in fluid with space-filling uniform stratification.

There are intrinsic differences between these two configurations. First, the profiles of shear and stratification evolve similarly during the evolution of shear instabilities in the two-layer configuration since both have similar initial hyperbolic tangent profile. However, stratification can evolve differently from shear in a uniformly stratified fluid, For the same value of \(R \) at the centre of the shear layer, the density difference across the layer is larger in the case with uniform stratification. In other words, the average value of the stratification is larger, leading to differences in the evolution of turbulence. Furthermore, ambient stratification is large, leading to difference as the evolution of turbulence. Furthermore, ambient stratification is large raily into the far field. For example, in the problem of a moderately stratified shear layer adjacent to a pycnocline where the pycnocline \(N \) was varied in a DNS study, Pham, Sarka \(R \) Enricker (2009

DF Studio - PDF Editor for Mac, Windows, Linux. For Evaluation. https://www.goppa.com/pdfstudio

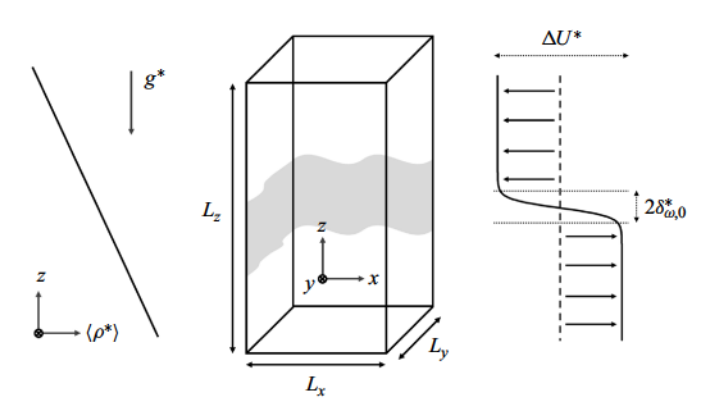


Figure 1. Sketch of the stratified shear layer with constant stratification.

during transition to fully three-dimensional turbulence. Previous simulations have shown TL with enhanced shear and stratification in the shear layer with uniform stratification (Pham *et al.* 2009; Watanabe *et al.* 2018). Simulations of the two-layer configuration also show formation of a TL although the enhancement of shear and stratification is significantly weaker (Mashayek & Peltier 2013). How the uniform stratification of the ambient can impact the development of the TL as well as the turbulence and mixing therein remains to be answered. Furthermore, the implications of the TL to mixing parameterizations requires thorough investigation.

This work is organized as follows. In § 2 the initialization and numerical formulation of the stratified shear layer is introduced. Section 3 provides a discussion of the evolution of the shear layer with specific emphasis on instabilities and subsequent turbulence. The structure of the TL, its turbulence and the wave flux across it are examined in § 4. A discussion of the mixing efficiency and its parameterization follows in § 5. The findings are discussed in § 6 and conclusions are drawn.

2. Formulation

2.1. Stratified shear layer

The problem of a temporally evolving stratified shear layer with uniform stratification is considered. A sketch of the shear layer with relevant initialization parameters is shown in figure 1. The flow is constructed with a streamwise velocity field given by

$$\langle u^* \rangle (z^*, t = 0) = -\frac{\Delta U^*}{2} \tanh\left(\frac{2z^*}{\delta_{\omega,0}^*}\right),\tag{2.1}$$

where ΔU^* denotes the velocity difference across the shear layer and $\delta_{\omega,0}^* = \Delta U^*/(\mathrm{d}\langle u^*\rangle/\mathrm{d}z^*)_{max}$ is the initial vorticity thickness. Note that a superscript * denotes a dimensional quantity while the $\langle \cdot \rangle$ operator indicates horizontal averaging.

Motivated by atmospheric and ocean observations in which stratification extends beyond regions of shear (Fritts 1982; Smyth, Moum & Caldwell 2001), this work utilizes a spatially extensive stratification. The density profile is initialized by a time-invariant uniformly stratified background density profile (ρ_b^*) . The background buoyancy frequency of the ambient fluid (N_0^{*2}) has a constant value given by $N_0^{*2} = -(g^*/\rho_0^*) \,\mathrm{d}\rho_b^*/\mathrm{d}z^*$, where g^* is gravity and ρ_0^* is a reference density.

Ri	L_x	L_{y}	L_z	$L_{z,sl}$	N_x	N_y	N_z	$\Delta(\times 10^{-3})$	Δ/η_{min}	k_0	δ_{TL}
0.04	12.96	6.48	32.32	$-3 \leqslant z \leqslant 3$	2304	1152	1408	5.62	2.2	0.97	0.84
0.08	11.86	5.93	32.18	$-2 \leqslant z \leqslant 2$	2048	1024	1024	5.79	2.0	1.06	0.81
0.12	11.12	5.56	32.18	$-2 \leqslant z \leqslant 2$	1920	960	1024	5.79	1.9	1.13	0.69
0.16	10.13	5.07	32.5	$-2 \leqslant z \leqslant 2$	1792	896	1024	5.65	1.9	1.24	0.59
0.2	9.52	4.76	32.5	$-2 \le z \le 2$	1536	768	1024	6.18	1.8	1.32	0.38

$$\frac{\partial u_j}{\partial x_i} = 0, (2.2a)$$

$$\frac{\partial u_i}{\partial t} + \frac{\partial (u_j u_i)}{\partial x_i} = -\frac{\partial p}{\partial x_i} + \frac{1}{Re} \frac{\partial^2 u_i}{\partial x_i \partial x_i} - Ri\tilde{\rho}g_i, \tag{2.2b}$$

$$\frac{\partial \tilde{\rho}}{\partial t} + \frac{\partial (u_j \tilde{\rho})}{\partial x_j} = \frac{1}{Re \, Pr} \frac{\partial^2 \tilde{\rho}}{\partial x_j \partial x_j} - w. \tag{2.2c}$$

$$Re = \frac{\Delta U^* \delta_{\omega,0}^*}{\nu^*}, \quad Ri = \frac{N_0^{*2} \delta_{\omega,0}^{*2}}{\Delta U^{*2}}, \quad Pr = \frac{\nu^*}{\kappa^*}.$$
 (2.3*a-c*)

Chongsiripinyo & Sarkar 2018). The Williamson low-storage, third-order Runge–Kutta method is employed for time advancement while the discretization of spatial derivatives is achieved using a second-order, central finite difference scheme. The Poisson equation for pressure is solved using a parallel multigrid solver. The streamwise and spamwise directions have periodic boundary conditions. In the vertical direction, vertical velocity has a homogeneous Dirichlet boundary condition while homogeneous Neumann boundary conditions are enforced for horizontal velocity components, density deviation and pressure. In a sponge region near the vertical boundaries in the regions z > 10 and z < 10 (sufficiently far from the shear layer), a Rayleigh damping function gradually relaxes the density and velocities to their corresponding boundary values in order to damp propagating fluctuations and prevent reflections of features such as internal waves which have propagated far from the shear layer.

For this work, an isotropic grid is used in the central region of the shear layer with a grid spacing of $\Delta x = \Delta y = \Delta z = \Delta$ as indicated in table 1. The streamwise and spanwise grids have uniform spacing while multi stretching is seld in the vertical outside the shear layer. Throughout the entire grid, the grid spacing is less than 2.2 η , where $\eta = (v^3/c)^{1/4}$ (de denotes turbulent Kinetic energy dissipation rate) is the Kolmogorov length scale, thus indicating appropriate resolution for capturing small-scale fluctuations. The number of grid points in the streamwise grid with every complete two wavelengths of the most unstable Kelvin-Helmholtz (K-H) mode in the streamwise directions are given by (N_x, N_y, N_y) and the domain extent is given by (N_x, N_y, N_z) and the domain extent is given by (N_x, N_z, N_z) as denoted in table 1. The computational domain is large enough to accommodate two wavelengths of the most unstable Kelvin-Helmholtz (K-H) mode in the streamwise directions are required in order to accurately ca

Turbulent shear layers in a uniformly stratified background

Here, the LSA is performed, taking into account the effect of viscosity, diffusivity and a finite domain, to examine the FGM when the shear layer is uniformly stratified. The theory and numerical implementation of the LSA is given in Smyth, Moum & Nash (2011). In the LSA, the Reynolds number, Prandtl number and domain size (L_2) have the same values as in the DNS. The grid spacing is $\Delta z = 0.025$. Free-slip and fixed buoyancy conditions are used at the top and bottom boundaries. The LSA of the two-layer profile is also performed for comparison.

Figure 2(ab) contrasts the mean profiles of the squared buoyancy frequency (N^2) , squared rate of shear (S^2) and gradient Richardson number (R_b) in the two-layer shear layer to those in the linearly stratified shear layer. The same level of stratification at the centre of the shear layer, $N^2 = 0.12$, is used. Away from the centre, N^2 decreases to zero in the two-layer case while it remains constant in the other case. As a result, R_b in the two-layer case while it remains constant in the other case. As a result, R_b in the two-layer case while it remains constant in the other case. As a result, R_b in the two-layer case is maller than that in the case with linear stratification throughout the shear layer is significantly higher in the case with linear stratification throughout the growth rate of the K-H shear instability.

Results of the LSA are shown in figure $2(c_d)$. In the two-layer case, the growth rate (σ) is similar to that of Hazel (1972) in the region with low k and R_b However, as k and R_b increase, the growth rate becomes slightly smaller than the value from Hazel (1972) due to the effect of viscosity, diffusivity and a finite domain. The location of PGMs (marked by a white line) in $k_{boc} - R_b$ space indicates a significant difference between the two configurations. While the wavenumber of the K-H modes varies little with R_b in the velocity, density and pr

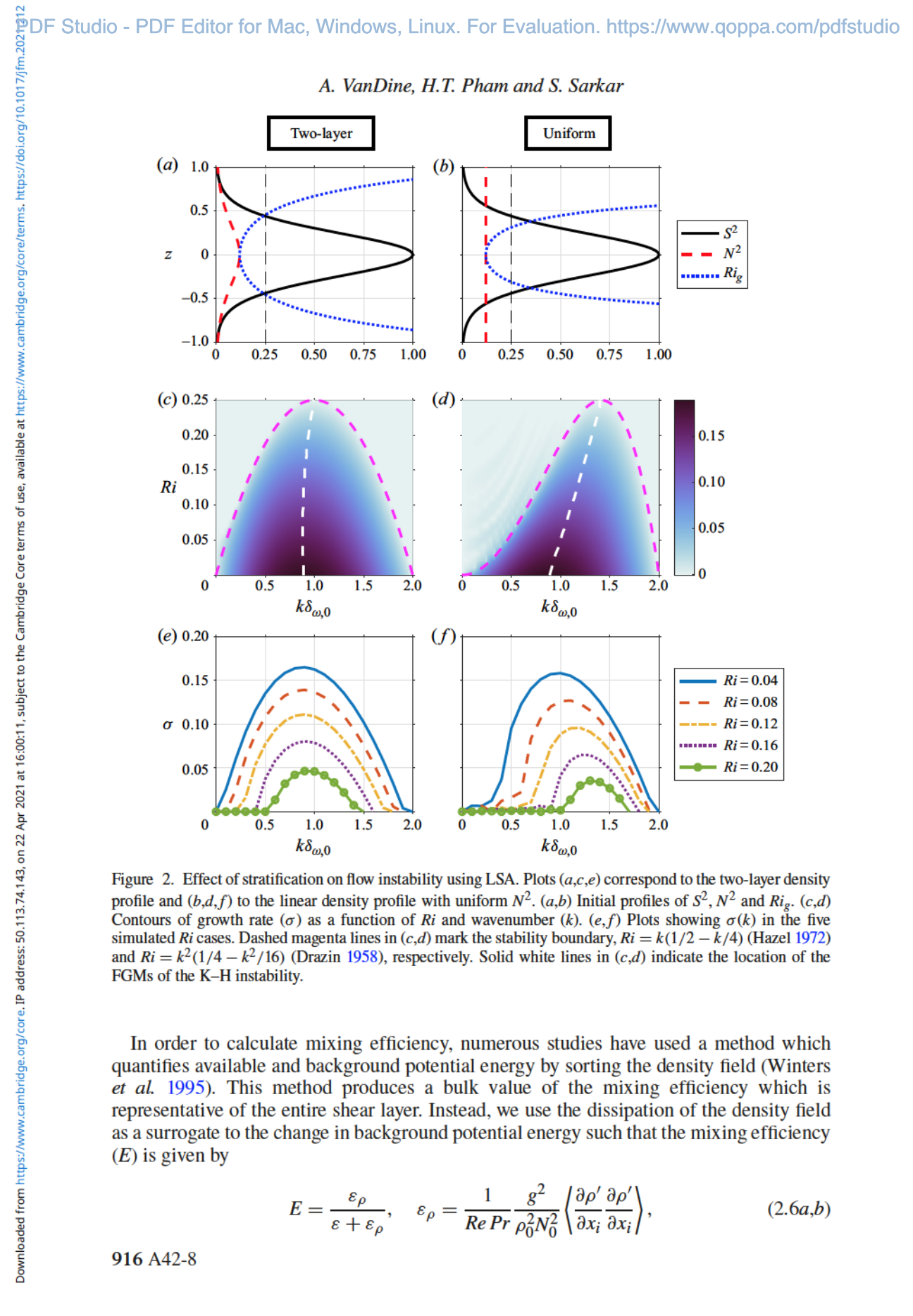
$$\frac{\mathrm{D}K}{\mathrm{D}t} = P - \varepsilon + B - \frac{\partial T_3}{\partial z},\tag{2.4}$$

$$K = \frac{1}{2} \left(\langle u' \rangle^2 + \langle v' \rangle^2 + \langle w' \rangle^2 \right),$$

$$P = -\langle u'w' \rangle \frac{\partial \langle u \rangle}{\partial z}, \quad \varepsilon = \frac{2}{Re} \langle s'_{ij} s'_{ij} \rangle, \quad s'_{ij} = \frac{1}{2} \left(\frac{\partial u'_i}{\partial x_j} + \frac{\partial u'_j}{\partial x_i} \right),$$

$$B = -Ri \langle \rho'w' \rangle, \quad T_3 = \frac{1}{2} \langle w'u'_i u'_i \rangle + \frac{1}{\rho_0} \langle w'p' \rangle - \frac{2}{Re} \langle u'_i s'_{3i} \rangle.$$

$$(2.5)$$



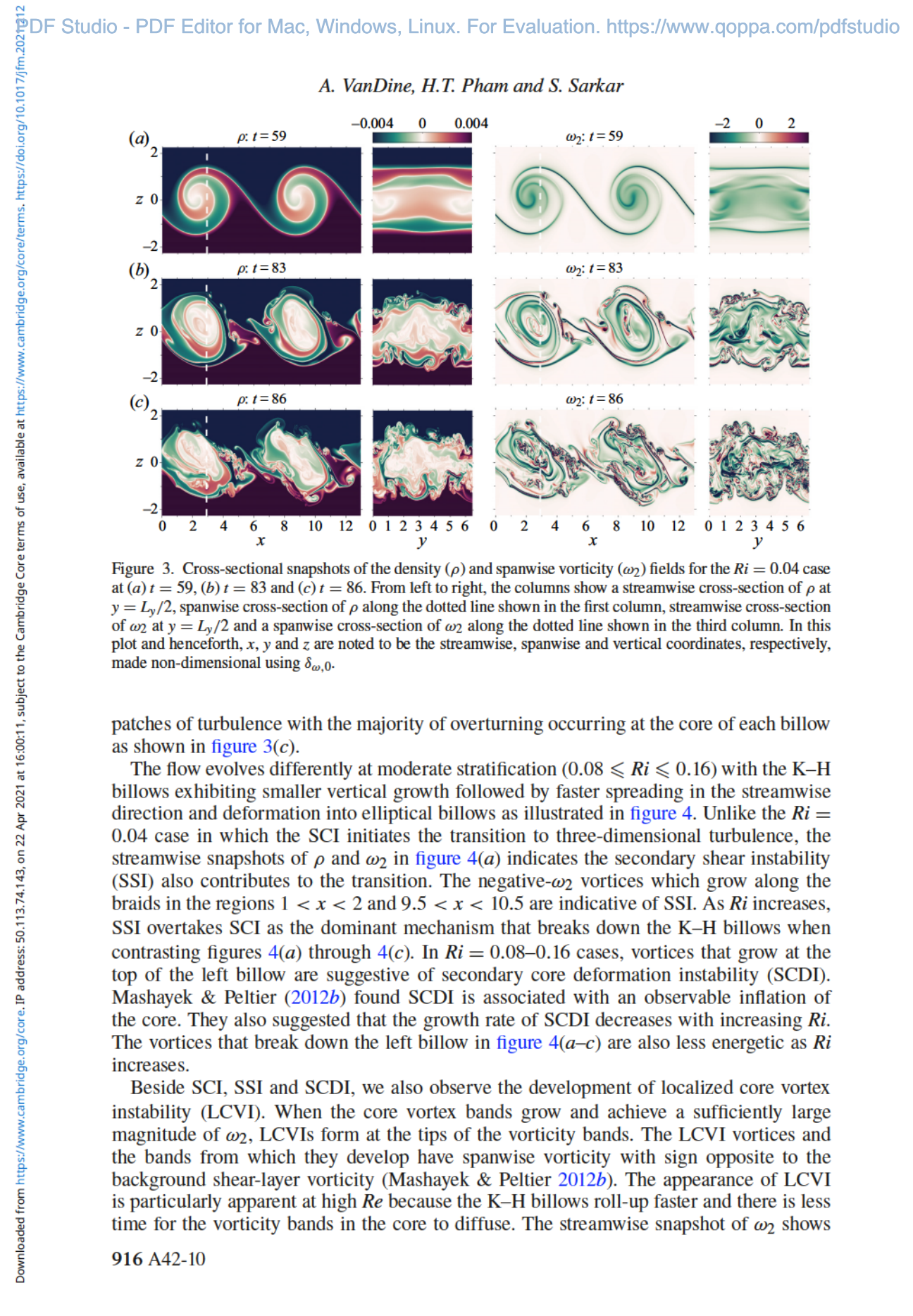
$$E = \frac{\varepsilon_{\rho}}{\varepsilon + \varepsilon_{\rho}}, \quad \varepsilon_{\rho} = \frac{1}{Re \, Pr} \frac{g^2}{\rho_0^2 N_0^2} \left\langle \frac{\partial \rho'}{\partial x_i} \frac{\partial \rho'}{\partial x_i} \right\rangle, \tag{2.6a,b}$$

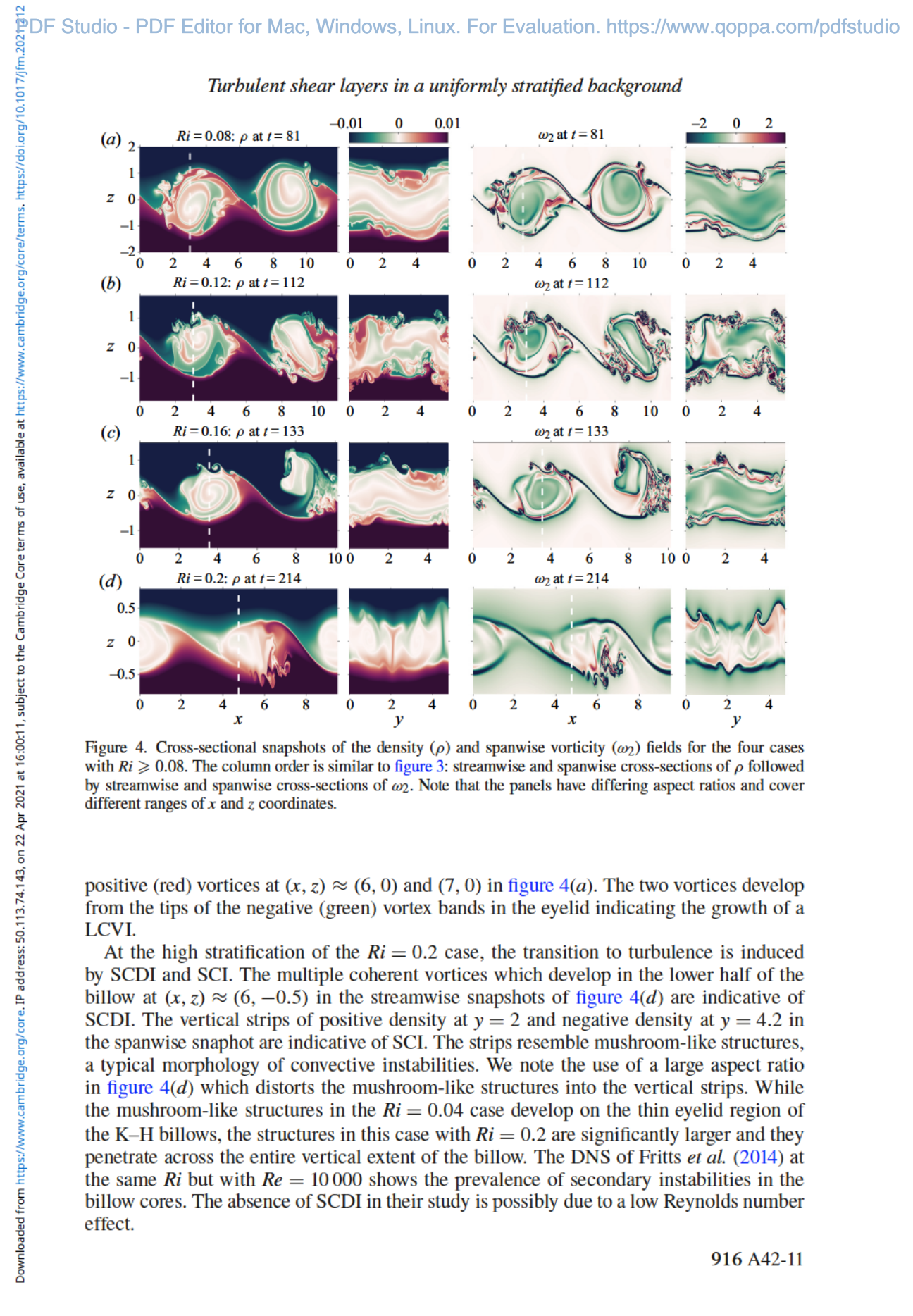
Turbulent shear layers in a uniformly stratified background where s_ρ is the dissipation rate of turbulent available potential energy (TAPE = $g^2(\rho^2)/2a_0^2N_0^2$). Scotti & White (2014) have demonstrated that this method of computing the mixing efficiency produces accurate results for turbulence in a continuously stratified fluid. Furthermore, this method is able to provide the spatial variability of the mixing efficiency throughout the shear layer as opposed to a single bulk value.

3. Flow evolution

3.1. Routes to turbulence: K–H shear instability and secondary instabilities

In a shear layer with inflectional shear it is understood that there is a strong primary instability in the form of a K–H shear instability. This instability manifests as a series of vortices which roll up over time (termed billows) and are connected by vorticity filaments (termed braids). As the K–H billows evolve, secondary instabilities develop throughout the shear layer (Mashayek & Peliter 2012a.b; Thorpe 2012; Arratia, Caulfield & Chomaz 2013; Salehipour et al. 2015). In the following discussion we use the visualization of density and vorticity fields to illustrate that, as in the shear layer between two layers of constant density, the continuously stratified shear layer exhibits rich dynamics of secondary instabilities. In the present study we do not perform LSA for each type of instability is excondary instabilities. Our identification of secondary instabilities is based on visual inspection and comparison with previous work in the two-layer problem. It is also noted that pairing of K–H billows is not found at the high Re of the present study. At sufficiently high Re, secondary instabilities hear layer, and differences between the various Ri cases are discussed thereafter. Figure 3 shows cross-sectional snapshots of the density (ρ) and spanwise vorticity ($\alpha_2 = 3a_1/3b_2 - 3a_2/3b_1$), Specific snapshots in time are shown where the time (ρ) represents the non-dimensional time, $S_0^{\mu \nu}$, where S_0^{μ} is the initia





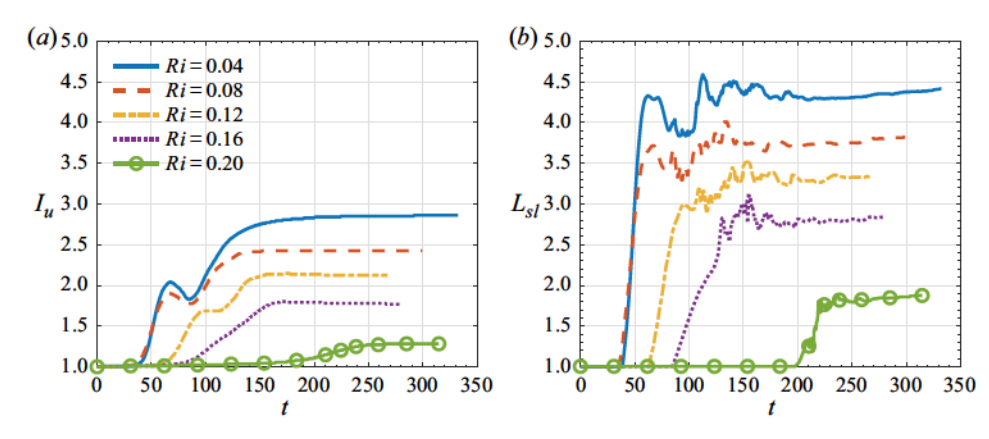


Figure 5. Temporal evolution of (a) momentum thickness (I_u) and (b) shear-layer thickness (L_{sl}) defined by the outer edges of the TL.

There are multiple modes that have similar vorticity manifestation such as the stagnation point instability (SPI) and secondary vortex band instability (SVBI). In fact, Mashayek & Peltier (2013) found that SVBI is a combination of both SPI and LCVI. Therefore, it is difficult to differentiate LCVI from SVBI without performing the stability analysis. Furthermore, the growth of secondary instabilities is highly sensitive to the initial broadband velocity fluctuations (Dong et al. 2019). We have simulated the Ri = 0.16 case with two different choices for the initial velocity perturbations: one where the energy spectrum peaks at $k_0 = 1.13$ and another with a peak at $k_0 = 1.24$. The horizontal domain length is chosen to accommodate two wavelengths of the most energetic mode in the initial velocity perturbations. While the evolution of the shear layer is statistically similar between the two cases, we find SPI to develop in only the former simulation with $k_0 = 1.13$ and not the latter. The SPI manifests as a single vortex which develops at the stagnation point in the braid. Overall, with regard to the secondary instabilities, the transition to turbulence in the shear layer with uniform stratification is as dynamically rich as that observed in the case with a two-layer density profile. Readers should be aware that there are other secondary instabilities that have not been observed in either Mashayek & Peltier (2013) or the present study such as knot and tube instabilities (Thorpe 2012).

3.2. Effect of stratification on the growth of shear-layer thickness

The visualization of the evolving shear layer suggests that the thickness of the shear layer varies significantly with the stratification. Here, we quantify the thickness of the shear layer through two quantities: (1) the momentum thickness (I_u) and (2) the layer bounded by the outer edges of the TLs denoted by L_{sl} . The first quantity provides an integral length scale which is used to compute non-dimensional numbers such as the bulk Richardson number, an important parameter typically used in the parameterization of shear-driven turbulence (Smyth & Moum 2000; Mashayek, Caulfield & Peltier 2017a). In contrast, the second quantity includes the mixing region at the edges of the shear layer. In the present study we identify the TL as a region with enhanced stratification (i.e. $N^2/N_0^2 > 1$) formed at the edge of the shear layer due to vertical turbulent transport from the core of the shear layer to its edge. Figure 5 indicates a significant difference between the two quantities with L_{sl} up to 60 % larger than I_u in the Ri = 0.16 case at late time. In this section we focus the discussion on I_u and defer consideration of L_{sl} to the next section.

$$I_u = \int_{-10}^{10} \left[1 - 4 \langle u \rangle^2 \right] dz \tag{3.1}$$

Turbulent shear layers in a uniformly stratified background

The momentum thickness, which is defined as $I_u = \int_{-10}^{10} \left[1 - 4 \langle u \rangle^2 \right] \mathrm{d}x \qquad (3.1)$ has the imprint of distinct flow regimes. At early time (approximately 30 < t < 60 in the Ri = 0.04 and Ri = 0.08 cases, and 50 < t < 90 in the Ri = 0.12 case), the shear layer thickness rapidly due to the enlargement of the K-H billows. In all cases, except for the $Ri \geqslant 0.16$ cases, there is a period where the shear layer briefly shrinks or stops growing before resuming its growth (approximately 60 < t < 80 in the Ri = 0.04 and Ri = 0.08 cases, and 100 < t < 110 in the Ri = 0.12 case). At Ri = 0.12, the layer does not contract significantly as in the Ri = 0.04 and Ri = 0.08 cases, and 100 < t < 110 in the Ri = 0.12 case). At Ri = 0.12, the layer does not contract significantly as in the Ri = 0.04 and Ri = 0.08 cases, and 100 < t < 110 in the Ri = 0.12 case). At Ri = 0.12, the layer does not contract significantly as in the Ri = 0.04 and Ri = 0.08 cases, and 100 < t < 110 in the Ri = 0.12 case). At Ri = 0.12, the layer does not contract significantly as in the Ri = 0.04 and Ri = 0.08 cases, and 100 < t < 10 in the Ri = 0.04 cases in the Ri = 0.04 and Ri = 0.08 cases, and Ri = 0.08 cases, and Ri = 0.08 cases, and Ri = 0.08 cases and R

$$\frac{\mathrm{d}I_u}{\mathrm{d}t} = \int_{-10}^{10} -8 \, \frac{\partial \bar{K}}{\partial t} \mathrm{d}z. \tag{3.2}$$

$$\frac{D\bar{K}}{Dt} = -P - \bar{\varepsilon} - \frac{\partial \bar{T}_3}{\partial z},\tag{3.3}$$

$$\bar{\varepsilon} = \frac{1}{Re} \left(\frac{\partial \langle u \rangle}{\partial z} \right)^2$$
 and $\bar{T}_3 = \langle u \rangle \langle u'w' \rangle - \frac{1}{Re} \langle u \rangle \frac{\partial \langle u \rangle}{\partial z}$. (3.4a,b)

$$\frac{\mathrm{d}I_u}{\mathrm{d}t} = \int_{-10}^{10} -8 \,\frac{\partial \bar{K}}{\partial t} \,\mathrm{d}z \approx \int_{-10}^{10} 8P \,\mathrm{d}z,\tag{3.5}$$

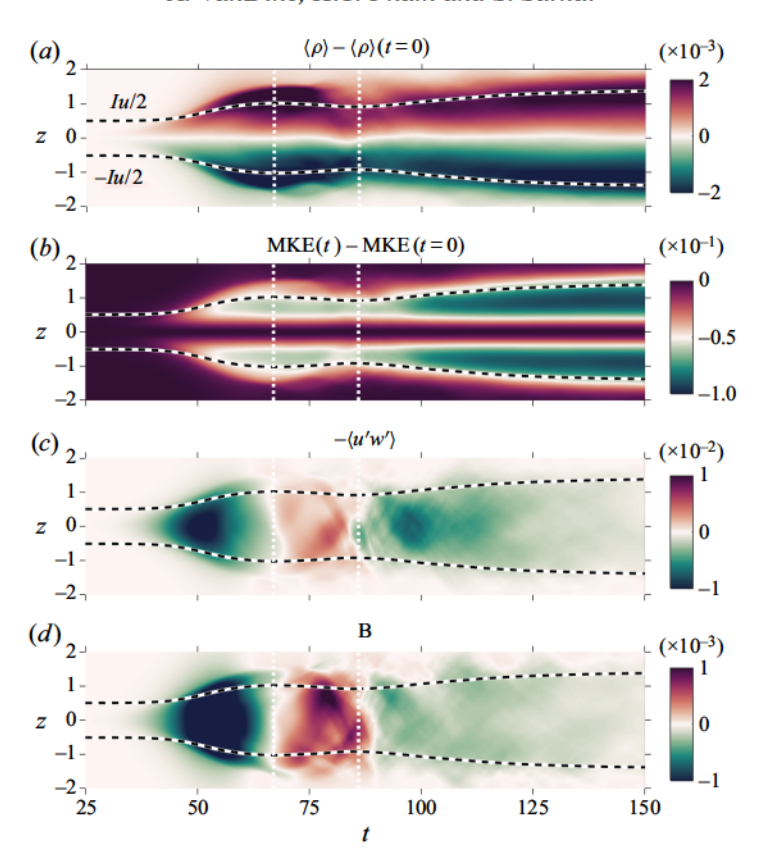
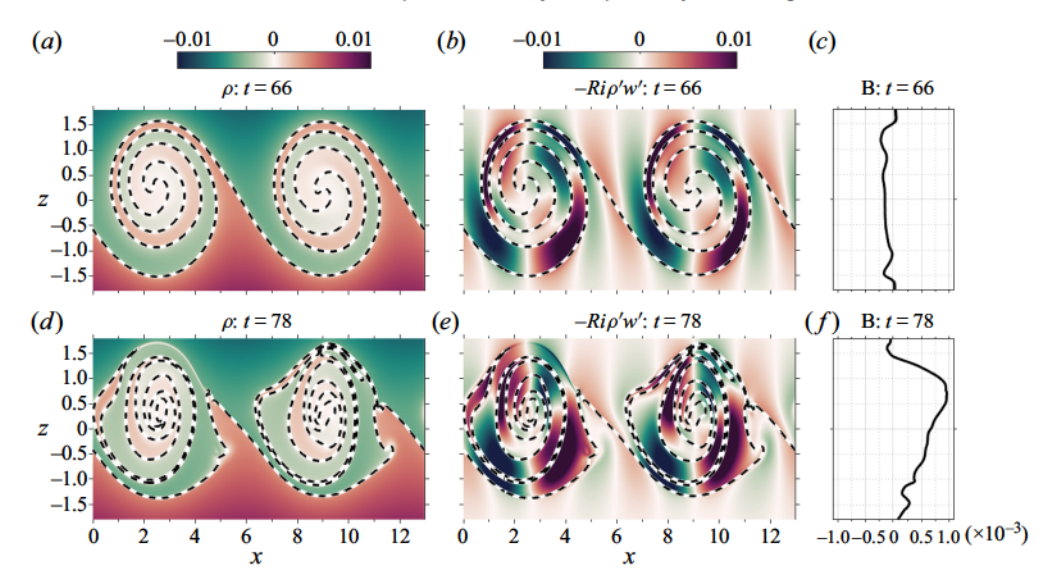


Figure 6. Evolution of the (a) density deviation from the initial profile, (b) MKE deviation from the initial profile, (c) momentum flux $(-\langle u'w'\rangle)$ and (d) buoyancy flux (B) for the Ri=0.04 case. Dashed lines denote the boundaries of the shear layer defined as $z=\pm I_u/2$. Vertical dotted white lines mark the contraction period of the momentum thickness.

downward, releasing the available potential energy that was previously gained. During this period, the MKE shown in figure 6(b) increases notably at the edges of the shear layer $(z = \pm 1)$. At the time when the shear layer begins to contract marked by the first vertical dotted white line in figure 6(c), the momentum flux $(-\langle u'w'\rangle)$ changes sign from negative to positive values signifying a counter-gradient momentum transport (CGMT). The CGMT occurs when the momentum flux does not follow the mean velocity gradient (Hussain 1986; Moser & Rogers 1993). Prior to the contraction, both the momentum flux and the mean velocity gradient have negative values, so the transport is down-gradient and the shear production is positive. In contrast, while the mean velocity gradient remains negative during the contraction, the momentum flux is counter-gradient and, thus, the negative production. After the contraction, the momentum transport reverts back to down-gradient and the production has positive values. Gerz & Schumann (1996) suggested that the energy of CGMT motions is provided by conversion of available potential energy to kinetic energy in homogenous stratified shear flows. Takamure et al. (2018) also found CGMT and negative production to occur in coherent vortices which develop during the transition from laminar to turbulent regimes in an unstratified mixing layer. It should be noted that contraction and CGMT were not observed in the DNS of a uniformly stratified shear layer at Re = 5000 and Ri = 0.05 (Pham & Sarkar 2010). It is interesting that the higher $Re = 24\,000$ in the present study would enhance the CGMT.

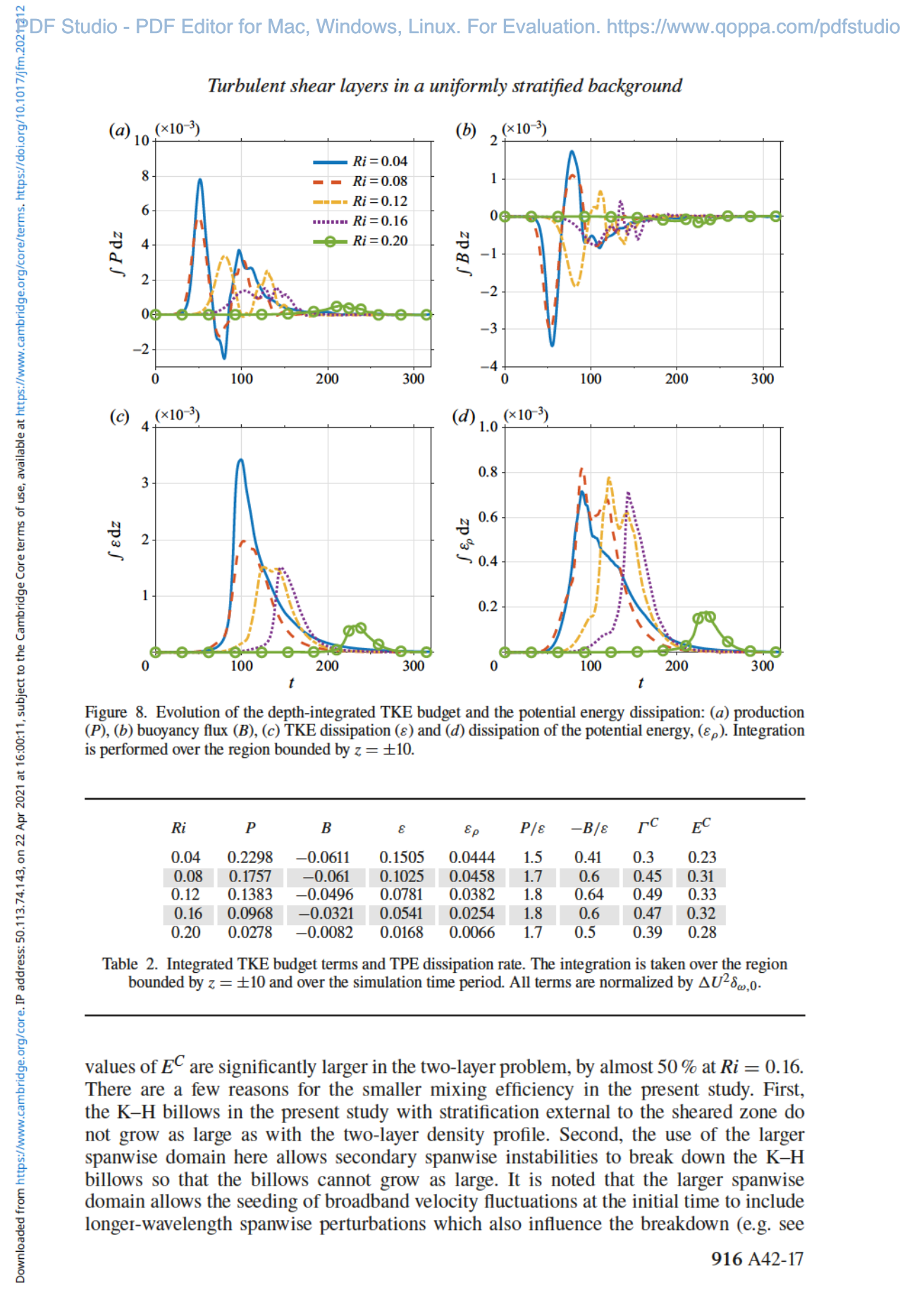


Turbulent shear layers in a uniformly stratified background $(a) = 0.01 \quad 0 \quad 0.01 \quad (b) \quad 0.01 \quad (c) \quad (c$

Who suggested the role of SCI becomes less important than SSI during the transition to turbulence at large Ri.

3.3. Effect of stratification on TKE budget and mixing efficiency

The evolution of depth-integrated terms in the TKE budget (figure 8) provides a comparison of turbulence energetics among the cases. The time for development of turbulence is substantially larger for the larger Ri, which is qualitatively consistent with the decrease of maximal growth rate with increasing Ri, shown previously in figure 2. The turbulent production P exhibits multiple peaks as time progresses, e.g. two distinct peaks in the cases with $Ri \le 0.12$. When the stratification is weak as in the Ri = 0.04 and Ri = 0.08 cases, the integrated production (figure 8a) has significant negative values and the buoyancy flux (figure 8b) has significant pose buoyancy flux (figure 8b) has significant pose to the CGMT and CGBF during the time interval of shear-layer contraction discussed in the previous section. It is after the contraction period that the shear layer becomes fully turbulent and the integrated e in figure 8(e) increases sharply. The largest peak value of integrated e occurs in the Ri = 0.04 case, while the peak values are comparable in the three cases with $0.08 \le Ri \le 0.16$. The peak value decreases significantly in the Ri = 0.0 case. Unlike the dissipation rate of the potential energy (e_p) in figure 8(d) develops earlier and during the contraction period. Noting that e is insignificant during the contraction period, Noting that e is insignificant during the contraction period, the fill lillows. A previously shown, during the deformation of the K-H billows, as previously shown, during the deformation of the K-H billows, density filaments/wisps inside the billows become significantly thinner. The filaments sharpen the density gradient in the shear layer down to the diffusive scale where it is dissipated by molecular diffusion. Interestingly, turbulence does not have a role in the



Ri	P	В	ε	$arepsilon_{ ho}$	P/ε	$-B/\varepsilon$	Γ^{C}	E^C
0.04	0.2298	-0.0611	0.1505	0.0444	1.5	0.41	0.3	0.23
0.08	0.1757	-0.061	0.1025	0.0458	1.7	0.6	0.45	0.31
0.12	0.1383	-0.0496	0.0781	0.0382	1.8	0.64	0.49	0.33
0.16	0.0968	-0.0321	0.0541	0.0254	1.8	0.6	0.47	0.32
0.20	0.0278	-0.0082	0.0168	0.0066	1.7	0.5	0.39	0.28

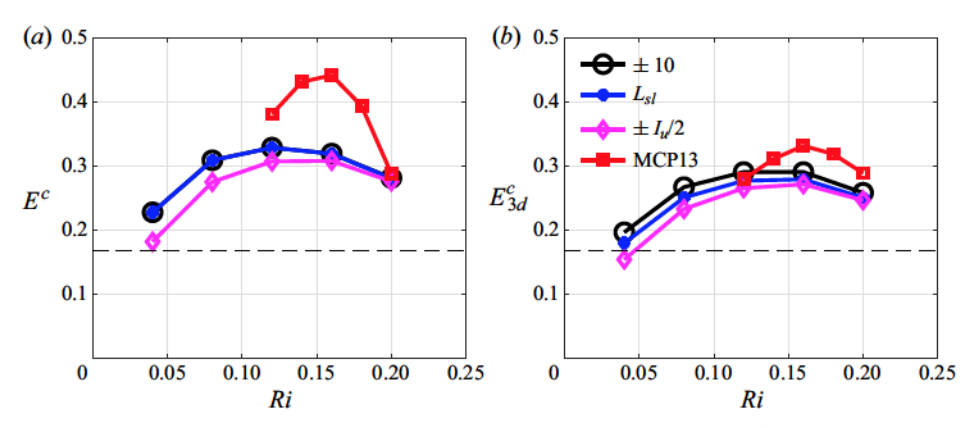


Figure 9. Effect of stratification on mixing efficiency after depth integration: (a) E^C computed by integrating ε_ρ and ε over the time duration of the simulations and (b) E^C_{3d} computed by starting integration from the time of fully developed turbulence indicated by the peak integrated dissipation rate. The depth integration is performed over the region bounded by the computational domain excluding the sponge layers $z=\pm 10$ (black), thickness of the shear layer L_{sl} (blue) and momentum thickness $\pm I_u/2$ (magenta). Mixing efficiency in the two-layer simulations (red) of Mashayek *et al.* (2013) (denoted MCP13) is shown for comparison. Dashed lines indicate the upper-bound value for the mixing efficiency suggested by Osborn (1980).

the spanwise snapshots in figure 3a). The study of Kaminski & Smyth (2019) indicates that strong turbulence in the shear layer at initial time can reduce the growth of K–H billows. Smaller K–H billows result in less available potential energy which is important for the subsequent turbulent mixing.

The mixing efficiency in the stage of three-dimensional turbulence (E_{3d}^{C}) is found by starting the integration from the time of peak integrated dissipation rate in figure 8(c). The maximum value of E_{3d}^{C} of 0.29 occurs in the Ri = 0.12 and 0.16 cases and is slightly smaller than the value seen in the two-layer problem. In the simulations with $Ri \ge 0.08$, when integrated across the shear layer and over time, the net dissipation rate decreases faster as Ri increases than the net scalar dissipation rate. The low mixing efficiency seen in the Ri = 0.04 case is due to the uniquely high TKE dissipation rate. It is noted that the cumulative mixing efficiency (E^C) and that due to fully developed turbulence (E_{3d}^C) are not dramatically different as reported in Mashayek et al. (2013). In other words, the mixing efficiency induced by the rich dynamics of the secondary shear instabilities during the transition to turbulence is only as significant as the subsequent fully developed turbulence. Nonetheless, both measures of the mixing efficiency are significantly larger than the upper-bound value of 1/6 proposed by Osborn (1980). While the mixing efficiency E^{C} is similar between the Ri = 0.08 and 0.2 cases, the integrated dissipation and scalar dissipation rates listed in table 2 are approximately seven times smaller in the case with stronger stratification. A large value of E^{C} does not imply large net mixing by K–H billows or turbulence.

4. The transition layer

As illustrated in the previous section, shear instabilities and the resulting turbulence transport a significant amount of momentum and energy toward the edges of the shear layer. These turbulent fluxes induce the formation of a TL in which the local stratification $N^2(z)$ and shear S(z) peak. Figure 9 suggests turbulent mixing in the TL can influence the overall mixing efficiency across the entire shear layer. When the dissipation and

Turbulent shear layers in a uniformly stratified background scalar dissipation rates are integrated over the shear-layer momentum thickness, i.e. $\pm l_u/2$, both E^C and E^C_{sd} have smaller values than when they are integrated over the shear-layer thickness defined by the TL (t_{sd}). Including the TL physics into the computation of mixing efficiency can increase E^C_{sd} by 17% in the $R^2 = 0.04$ case. Furthermore, internal waves are generated inside the TL and it is unclear how the wave excitation affects the mixing efficiency (Watanabe a al. 2018). Therefore, it is important to understand how turbulence and wave physics in the TL influence the mixing efficiency and its parameterization.

While the mixing efficiency is significant ($E^C = 0.28$) in the $R^1 = 0.2$ case, the net dissipation and scalar dissipation are are considerably smaller than in the other cases as listed in table 2. Because of the lack of vigorous mixing in the $R^1 = 0.2$ case and, for brevity, we exclude this case from the following discussion of the TL.

Each of the two edges of the shear layer has a TL. For the purposes of this work, the boundaries of a TL are defined using the normalized squared buoyancy frequency, N^2/N_0^2 , whose evolution is shown in figure 10. The inner and outer boundaries of the TL are demarcated by N^2/N_0^2 = 1 such that the interior of the TL has N^2/N_0^2 > 1. Since the layer of enhanced N^2 first develops near the centre of the shear layer during the early stage of growing K-H instability, we use $I_{st}/2$ to mark the inner boundary of the TL. Note that the location of maximum N^2/N_0^2 (magenta dashed line in figure 10) varies; it is closer to the inner boundary of the TL at early time and located more centrally between the two boundaries at late time. There is a sharp increase of N^2/N_0^2 in the lower half of the TL before and during the growth stagnation/contraction regime for the $R^1 \le 0.12$ cases. In all cases, as the flow transitions from being dominated by two-dimensional

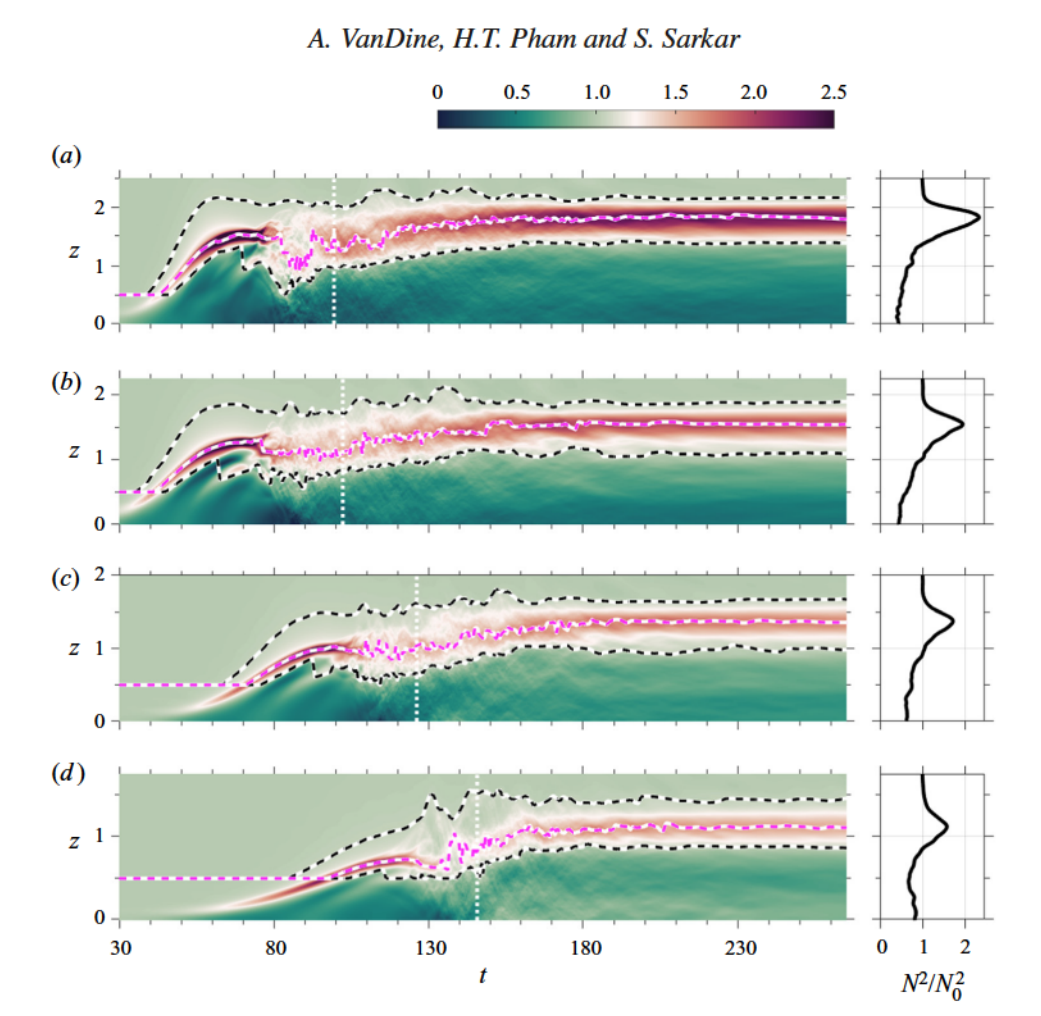


Figure 10. Evolution of the normalized squared buoyancy frequency (N^2/N_0^2) shown using t-z contours for the (a) Ri=0.04, (b) Ri=0.08, (c) Ri=0.12 and (d) Ri=0.16 cases. The inner (TL_i) and outer (TL_o) TL boundaries are each identified using a black dashed line while the location of maximum N^2/N_0^2 inside the shear layer (TL_m) is shown with a magenta dashed line. Panels are given on the right for each case to illustrate vertical profiles of N^2/N_0^2 at $t\approx 250$ when the turbulence has subsided. The dotted white lines in all panels indicate the time of maximum dissipation rate (t_{3d}) .

time is located in the TL, close to its inner boundary, with TL shear intensity among cases increasing with strengthening N_0 . At early time in all cases, a region of strong shear directly corresponds to the region of large N^2/N_0^2 in the TL. The previously discussed reduction in N^2/N_0^2 coincides with a brief reduction in shear in the Ri = 0.04 and Ri = 0.08 cases. In the more strongly stratified cases there is less significant reduction in shear. At late time in the highly stratified cases, S^2 has a layered structure similar to N^2 . The panel to the right of figure 11(d) shows the centre of the shear layer to have a region of moderate shear bounded by a layer of weaker shear. Farther from the centre, S^2/S_0^2 increases to a peak value of approximately 0.23 before becoming negligible outside the TL.

Figure 12 shows the gradient Richardson number $(Ri_g = N^2/S^2)$ which is a measure of the balance between buoyancy and shear. In all cases, the inner portion of the TL has lower Ri_g than the outer half indicating that the inner portion is more influenced by effects of shear. As the flow evolves, turbulence mixes the density and momentum fields and Ri_g

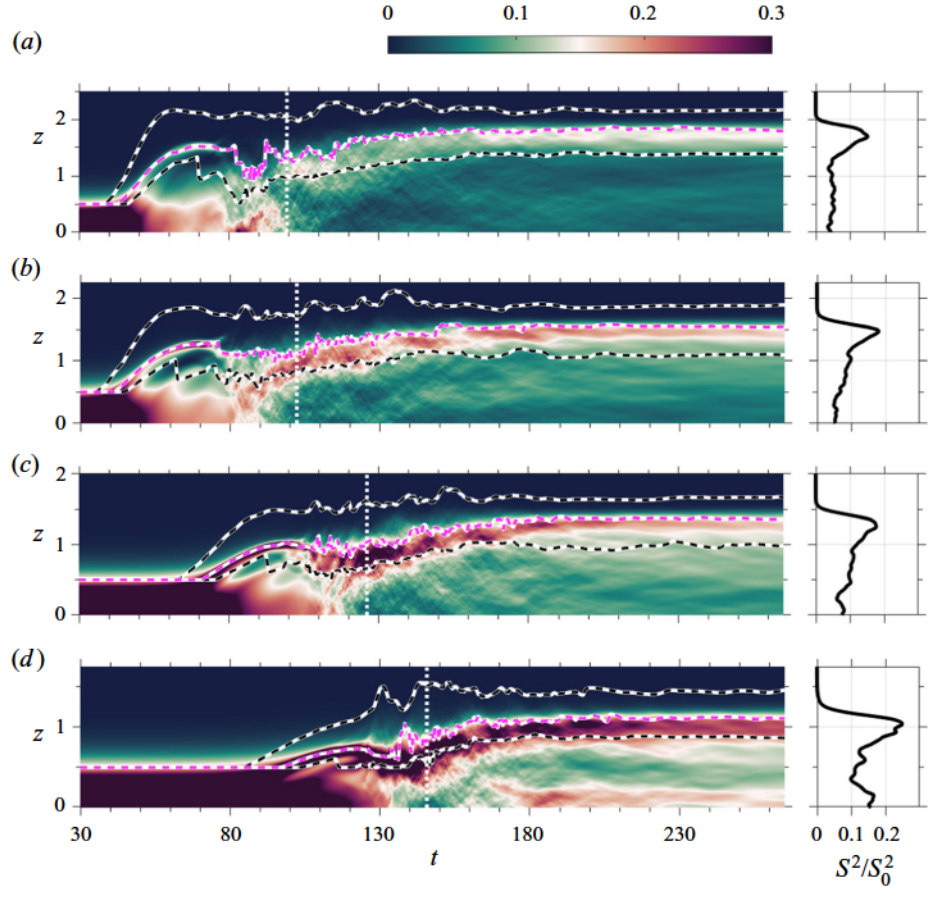


Figure 11. Similar to figure 10 but the contours show the normalized squared rate of shear (S^2/S_0^2) .

increases exceeding the critical value of 0.25 from linear stability theory (Hazel 1972). In all cases, this behaviour is observed within the TL with Ri_g beginning small and eventually becoming much larger than Ri_c . At late time, the interior of the shear layer is dominated by $Ri_g > 0.5$ in all cases except for the Ri = 0.04 case in which Ri_g takes values between $Ri_c = 0.25$ and 0.5. In the Ri = 0.12 case intermittent layers of $Ri_g > 0.75$ and $Ri_g > 1$ are observed, in contrast to the two-layer simulations of Mashayek & Peltier (2013) who noted that $Ri_g \approx 0.5$ across the entire shear layer at late time in their comparable simulation. The higher Ri_g found here is further evidence of the difference in the distribution of S^2 and N^2 between the present case of uniformly stratified background and the case with two constant-density layers.

The development of small-scale fluctuations as the flow becomes fully turbulent leads to a rapid increase in the dissipation rate (ε in figure 13). The time of peak ε , seen when the K–H billows breakdown to three-dimensional turbulence, is delayed with increasing background stratification (N_0^2) as follows: $t \approx 100$ in the Ri = 0.04 and Ri = 0.08 cases, $t \approx 126$ in the Ri = 0.12 case and $t \approx 145$ in the Ri = 0.16 case. Furthermore, as N_0^2 increases among cases, ε tends to be elevated in the TL at late time. Dissipation is strongest at the periphery near the inner boundary of the TL due to the evolving late-time instabilities.

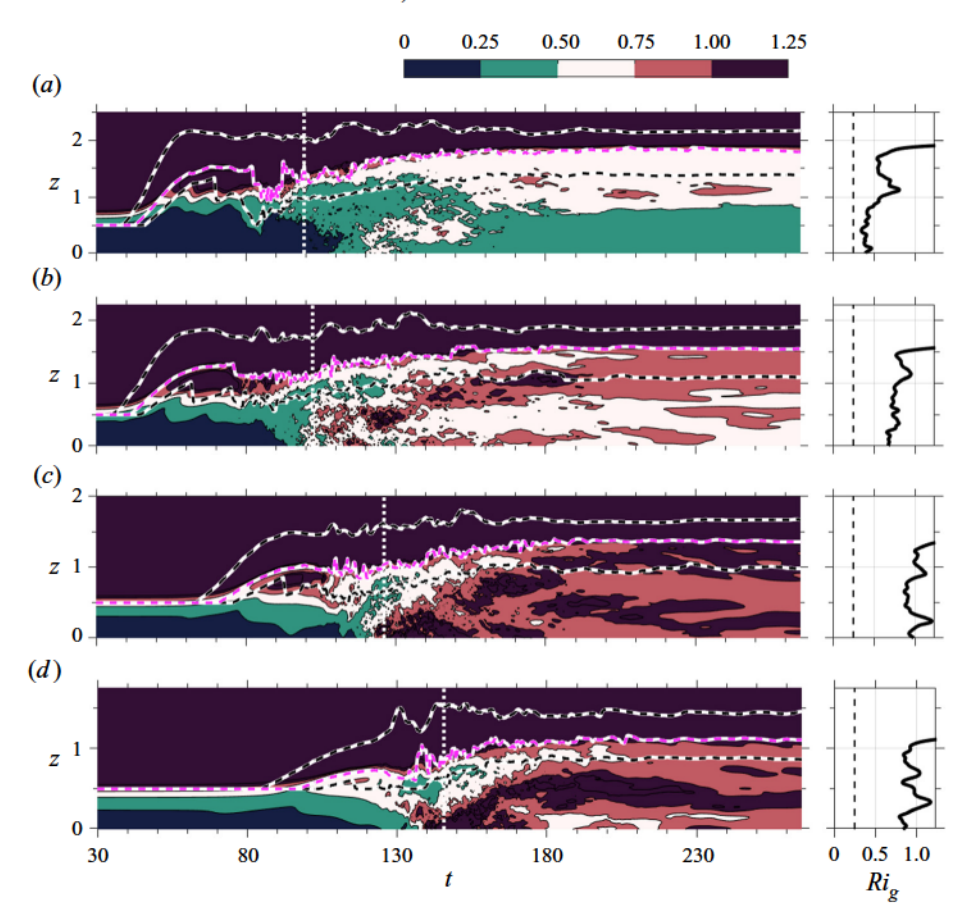
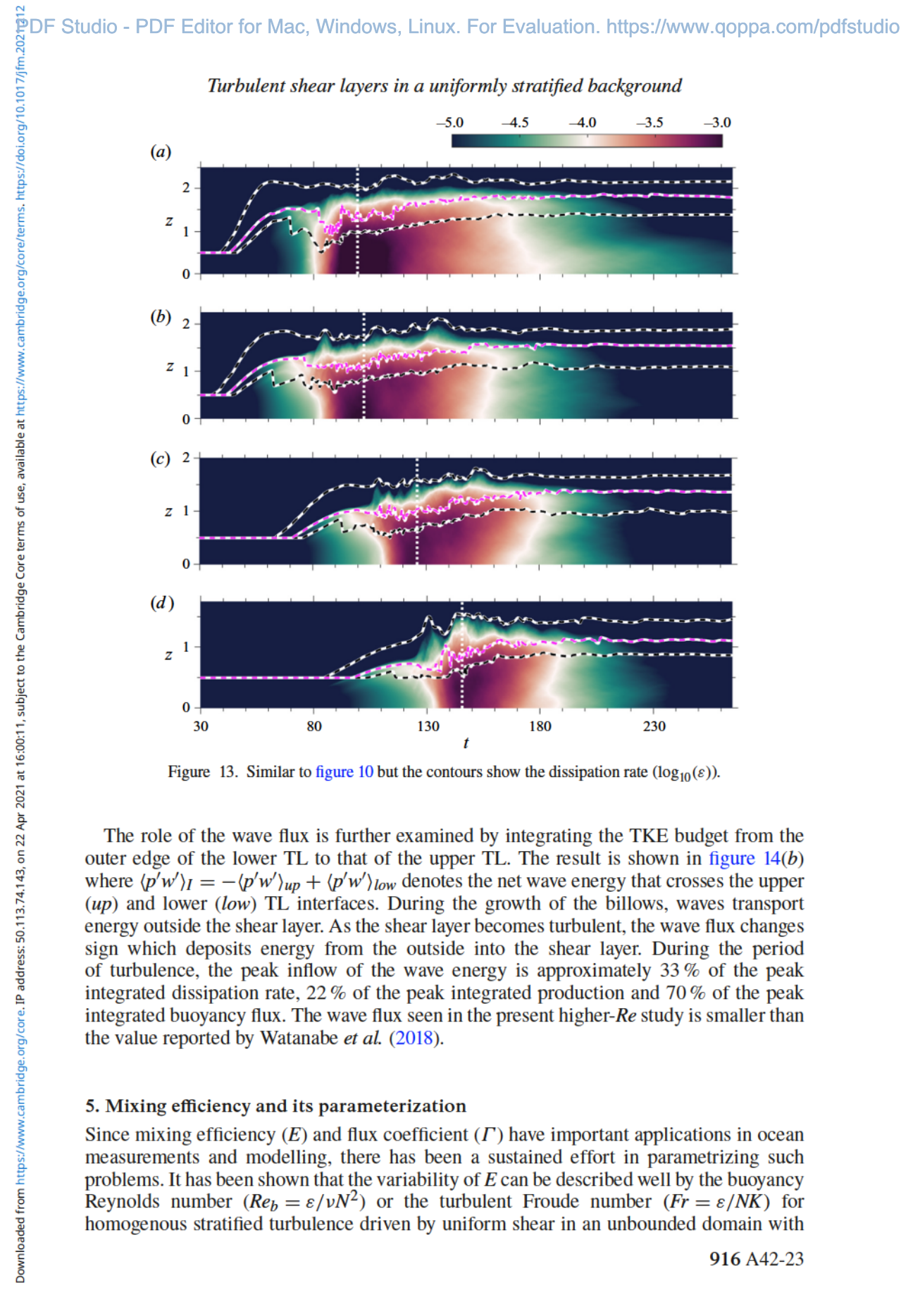


Figure 12. Similar to figure 10 but the contours show the gradient Richardson number (Ri_g) .

4.2. Internal wave flux across TLs

Simulations by Watanabe et al. (2018) at Re = 6000 and Ri up to 0.08 suggest the internal wave flux, $\langle p'w' \rangle$, at the TNTI to be strong. They report that the wave energy flux at the TNTI can be comparable to the dissipation in the shear layer. It is of interest to compare the role of $\langle p'w' \rangle$ at the shear-layer edge as the Reynolds number increases from 6000 to 24 000. Figure 14(a) illustrates the evolution of $\langle p'w' \rangle$ in the Ri = 0.08 case in which its magnitude is largest during the transition from two-dimensional K-H billows to three-dimensional turbulence. As the billows grow, they create perturbations in the pressure and velocity fields that extend beyond the boundaries of the shear layer (denoted by the dashed lines in figure 14a). The perturbations generate evanescent waves whose amplitude decays exponentially with the distance away from the shear layer. The wave flux is initially positive in the upper shear layer and negative in the lower shear layer, and as a result, TKE is transported away from inside the shear layer to the outside during the growth of the K-H billows. It is noted that, since the waves are evanescent, energy does not propagate into the far field. As the shear layer grows in size, the energy that was previously transported outside contributes to the turbulent mixing in the TL. The internal wave flux in the TL is significantly weaker when the shear layer is turbulent.



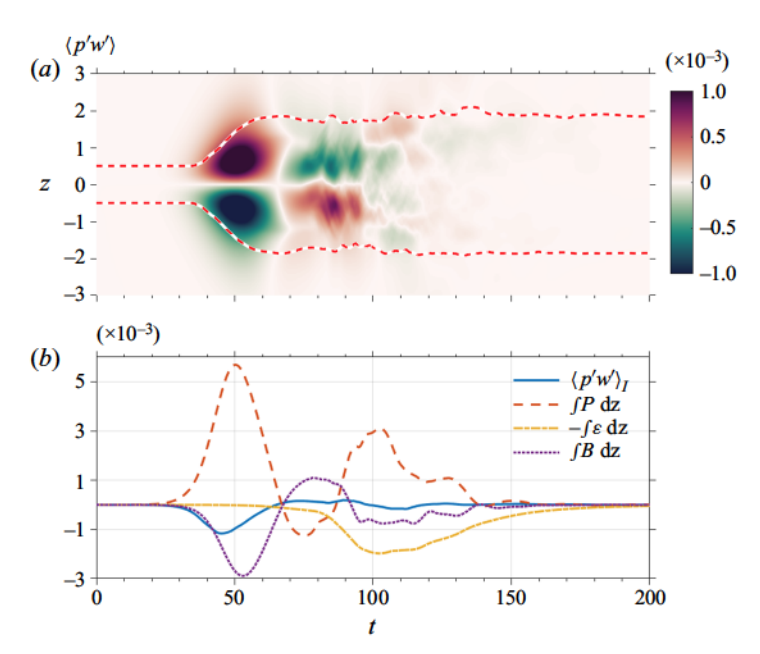


Figure 14. Internal wave flux and its influence on the TKE budget for the Ri = 0.08 case: (a) temporal evolution of $\langle p'w' \rangle$, and (b) a comparison of the net internal wave flux across the upper and lower TLs (the dashed boundaries shown in (a)) given by $\langle p'w' \rangle_I$ with respect to the other terms in the integrated TKE budget. Dashed lines in (a) denote the outer edges of the TLs.

uniform N (Shih *et al.* 2005; Ivey, Winters & Koseff 2008; Garanaik & Venayagamoorthy 2019). The mixing efficiency E is found to also depend on Pr and Ri (Salehipour & Peltier 2015; Salehipour *et al.* 2015). Salehipour *et al.* (2016) proposed a mixing parameterization that is based on Re_b and Ri while Mashayek *et al.* (2017b) suggested a parameterization that only relies on Re_b . In the following discussion we examine the spatial variability of E in the present configuration of a localized shear layer in a uniformly stratified fluid and discuss the results in light of the parameterization schemes proposed in the aforementioned studies. Since Pr = 1 here, only the dependence on Re_b , Fr and Ri are to be explored.

We find that the strong TL associated with the present configuration plays an important role through its mixing during the later-time period of decaying TKE. The significant turbulent activity in the TL is illustrated in figure 15 for the four cases with $Ri \leq 0.16$. Small-scale shear instabilities can be clearly seen in the vorticity field at times when the integrated turbulent dissipation across the shear layer is larger than the integrated production. These later-time shear instabilities grow and persist in the TL at the upper and lower edges of the shear layer and they contribute significantly to the bulk mixing in the shear layer. Therefore, it is critical for parameterization schemes to capture their effect.

Figure 16 shows the evolution of the mixing efficiency (E) given by (2.6a,b) with the boundaries of the TL also depicted. Overall, E is much higher throughout the shear layer as K–H billows are forming. As they break down into turbulence, strong E is seen at the outer boundary of the TL while the core of the shear layer becomes relatively quiet with low E. This large E occurs after the secondary peak in production in the low Ri cases and is associated with the concentration of TKE in lobed structures. The inner boundary of the TL has relatively low E. As stratification increases and buoyancy effects suppress vertical motions, E becomes smaller at early time as can be seen by comparing the Ri = 0.16 and

Turbulent shear layers in a uniformly stratified background

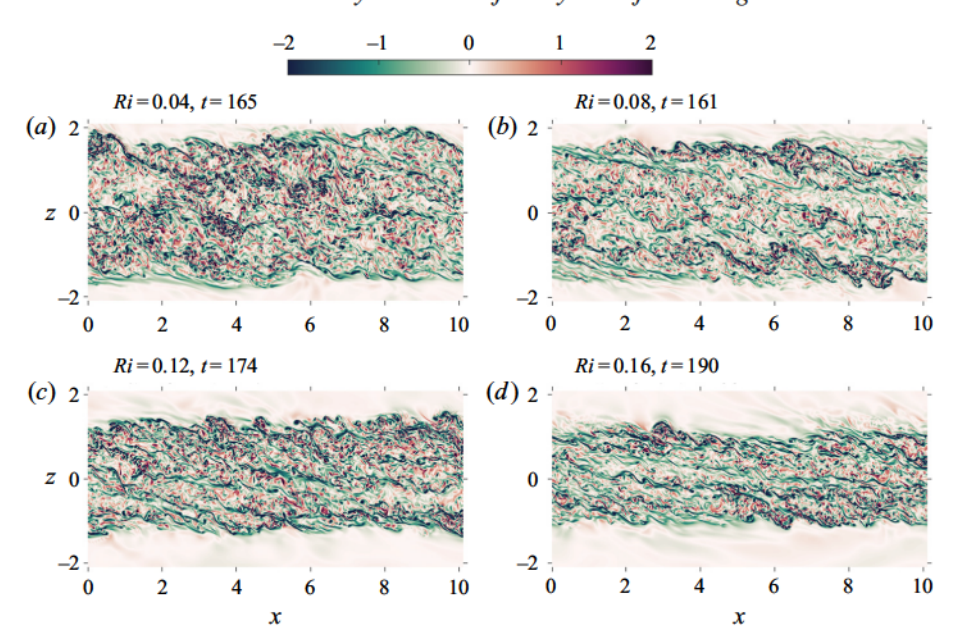


Figure 15. Cross-sectional snapshots of the spanwise vorticity (ω_2) fields for the (a) Ri = 0.04, (b) Ri = 0.08, (c) Ri = 0.12 and (d) Ri = 0.16 cases.

Ri = 0.04 cases in figure 16. At late time, the majority of high-efficiency mixing occurs within or above the TL.

To parametrize mixing efficiency, it is necessary to relate a bulk mixing efficiency to the bulk values of Reynolds number, Froude number and Richardson number. The time-dependent bulk values are obtained by integration across the shear layer from the outer edge of the bottom TL to that of the top TL. This choice of integration domain (thickness denoted by L_{sl}) encompasses the spatial region of significant turbulent dissipation. We also focus the analysis on the temporal period with significant mixing, namely the regime of fully developed turbulence which commences after the time of the peak integrated ε , similar to Salehipour *et al.* (2016) and Mashayek *et al.* (2017*b*). In the discussion to follow, the bulk mixing efficiency (E_{3d}), bulk buoyancy Reynolds number (Re_b), bulk turbulent Froude number (Fr) and bulk Richardson number (Ri_b) are computed as follows:

$$E_{3d}(t) = \frac{\int_{L_{sl}} \varepsilon_{\rho} \, dz}{\int_{L_{sl}} \varepsilon_{\rho} + \varepsilon \, dz}, \quad Re_{b}(t) = \frac{\int_{L_{sl}} \varepsilon \, dz}{\int_{L_{sl}} \nu N^{2} \, dz},$$

$$Fr(t) = \frac{\int_{L_{sl}} \varepsilon \, dz}{\int_{L_{sl}} NK \, dz}, \quad Ri_{b} = \frac{\Delta \rho_{sl} g L_{sl}}{\rho_{0} \Delta U_{sl}^{2}}.$$

$$(5.1)$$

Here $\Delta \rho_{sl}$ and ΔU_{sl} denote the density and velocity change across the spatial integration domain.

The dependence of mixing efficiency (E_{3d}) on Re_b is shown in figure 17(a). Shih et al. (2005) suggested three regimes of turbulent mixing: an energetic regime $(Re_b > 10^2)$,

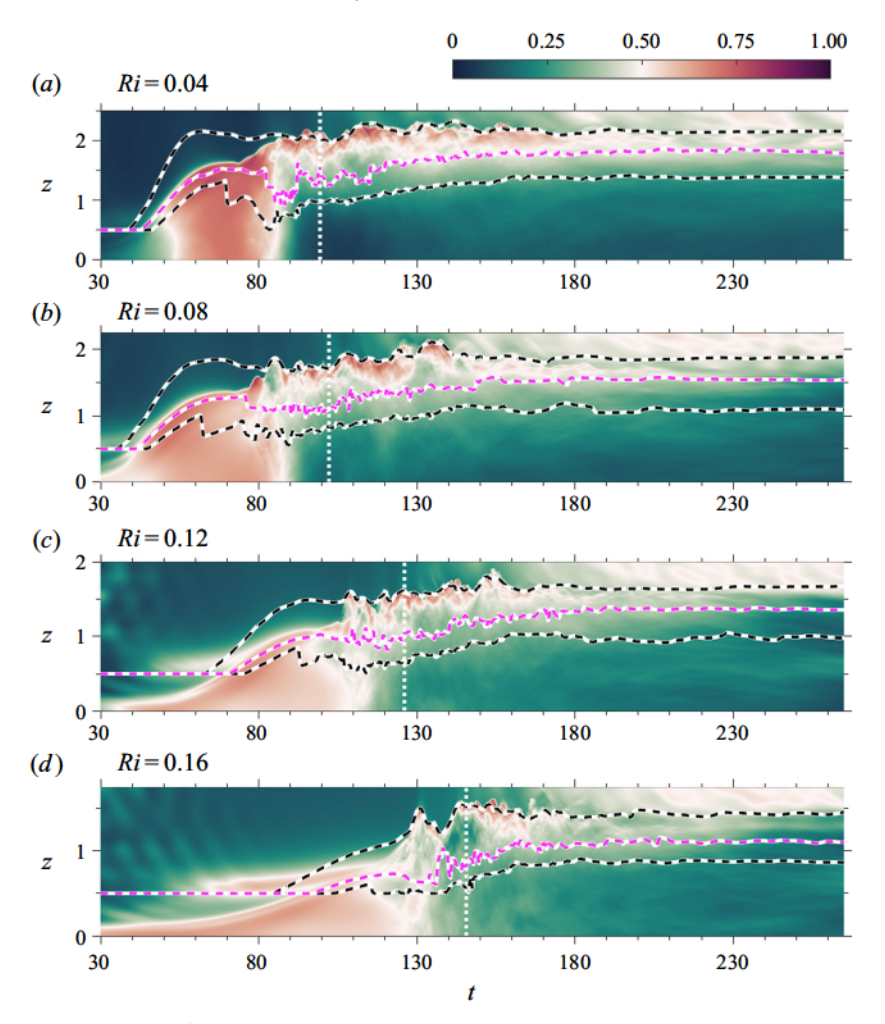


Figure 16. Similar to figure 10 but the contour shows the mixing efficiency (E).

an intermediate regime ($7 \le Re_b \le 10^2$) and a diffusive regime ($Re_b < 7$). These three regimes are also exhibited in the present study although the values of Re_b used to separate the regimes are slightly different. In the present study, E_{3d} decreases with increasing Re_b in the energetic regime (Re_b is as large as 540 in the Ri = 0.04 case). During the intermediate regime ($40 < Re_b < 100$), E_{3d} remains relatively constant at the value of 0.3 in the cases with $0.08 \le Ri \le 0.16$. The mixing efficiency decreases monotonically in the diffusive regime ($Re_b < 40$).

The flux coefficient (Γ_{3d}) is also often used to quantify mixing. From mixing efficiency, the flux coefficient can be computed as $\Gamma_{3d} = E_{3d}/(1-E_{3d})$. Figure 17(b) shows the flux coefficient also varies with Re_b in three distinctive regimes similar to the mixing efficiency. The peak value of Γ_{3d} is approximately 0.43 which is more than twice larger than the upper-bound value of 0.2 suggested by Osborn (1980). Furthermore, Γ_{3d} remains larger than 0.2 over the entire lifespan of turbulence in the cases with $Ri \ge 0.08$. The flux coefficient Γ_{3d} peaks at a smaller value of 0.32 in the Ri = 0.04 case and decreases to below 0.2 in the diffusive regime.

Turbulent shear layers in a uniformly stratified background

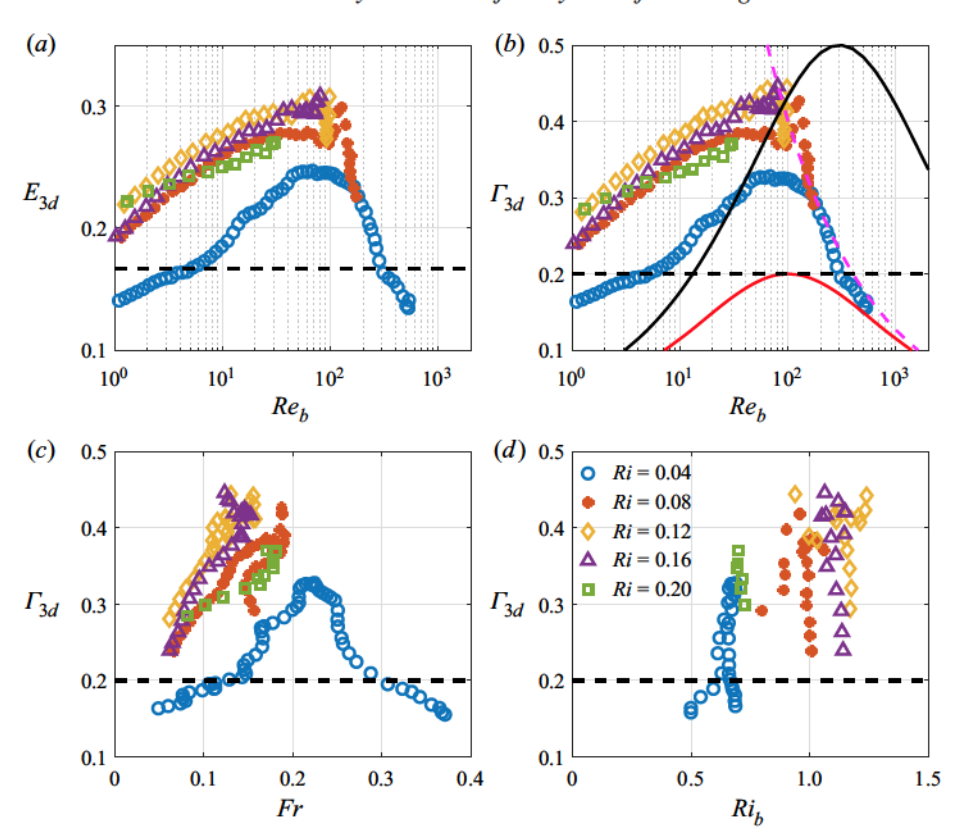


Figure 17. Effect of buoyancy Reynolds number (Re_b) on (a) mixing efficiency (E_{3d}) , and (b) flux coefficient (Γ_{3d}) and the effect of (c) turbulent Froude number (Fr) and (d) bulk Richardson number (Ri_b) on the flux coefficient during the turbulent phase. The dashed black lines indicate the values of $E_{3d} = 1/6$ and $\Gamma_{3d} = 0.2$ suggested by Osborn (1980). The dashed magenta line in panel (b) indicates the parameterization, $\Gamma_{3d} = 4Re_b^{-1/2}$ for $Re_b > 10^2$ in the Ri = 0.04 case. The solid black and red lines in panel (b) denote the upper and lower bounds, respectively, of the parameterization proposed by Mashayek *et al.* (2017*b*).

Shih *et al.* (2005) indicated that the flux coefficient decreases as $\Gamma_{3d} = 2Re_b^{-1/2}$ in the energetic regime. We also find that $\Gamma_{3d} \propto Re_b^{-1/2}$ in the Ri = 0.04 case although its value is substantially larger here leading to a proportionality coefficient of 4 as shown in figure 17(b). During the intermediate regime, the flux coefficient remains relatively constant with a value ranging from 0.33 in the Ri = 0.04 case to approximately 0.43 in the other three cases. These values are larger than that of 0.2 reported in Shih *et al.* (2005). While Shih *et al.* (2005) asserted that turbulent mixing in the diffusive regime is driven mainly by molecular diffusivity and independent of Re_b , the turbulent mixing in the present study is significantly higher than the molecular counterpart and, indeed, varies with Re_b when $7 \le Re_b \le 40$. Nonetheless, the mixing convention of Shih *et al.* (2005) is kept in the present study for ease of comparison.

The upper and lower bounds for Γ_{3d} suggested by Mashayek *et al.* (2017*b*) are also included in figure 17(*b*) for comparison. Inherently, the dependency of the flux coefficient on Re_b in the present study agrees better with the suggested parameterization using homogenous stratified turbulence in Shih *et al.* (2005) than the one in Mashayek *et al.* (2017*b*). In the latter scheme, Γ_{3d} peaks at a transitional Re_b with values ranging

A VanDine, H.T. Pham and S. Sarkar

from 100 to 300. As R_{b_0} increases in the shear-dominated regime or decreases in the buoyancy-dominated regime, Γ_{bd} decreases similarly at the same rate. The $Rl \leq 0.16$ cases in the present study indicate Γ_{bd} peaks at $R_{cb} \approx 10^2$ and, furthermore, it does not decrease similarly as R_{cb} deviates from the transitional value. The $Rl \leq 0.16$ cases shows the presence of an intermediate regime $(40 \leqslant R_{cb} \leqslant 10^2)$ in which Γ_{bd} remains relatively constant at values closer to the upper bound than the lower bound given by Mashayek et al. (2017b). We note that the parameterization suggested in Mashayek et al. (2017b) is based on both DNS of a shear layer with a two-layer density profile and observational data collected at sites where stratification and shear profiles are space-filling unlike their DNS set-up. It is unclear how the disparity between the DNS and the observational data influences the suggested parameterization. Nonetheless, the R_{cb} dependence of Γ_{3d} seen in the present study suggests further evaluation of the parameterization.

Beside R_{cb} , the turbulent Froude number (Pr(f)) can be a well-suited parameter for mixing parameterization of homogenous stratified turbulence (Ivey & Imberger 1991; Shih et al. 2000; Howland, Taylor & Caulifield 2020). The metric shows the competition between turbulent time scale (K_f) and buoyancy time scale (N^{-1}) so it can be used to describe the local state of stratified shear turbulence. For weakly stratified turbulence (Fr > 1), the flux coefficient decreases as Fr^{-2} while it remains relatively constant for strongly stratified turbulence (Fr > 1) (Garanaik & Venayagamoorthy 2019). In the present study we also observe two regimes of Fr as shown in figure 17(c). In the Ri = 0.04 case the two regimes are delineated by $Fr \approx 0.2$, a value somewhat smaller than unity. As Fr increases or decreases from this value, Fr decreases which suggests the optimal rate of mixing at F

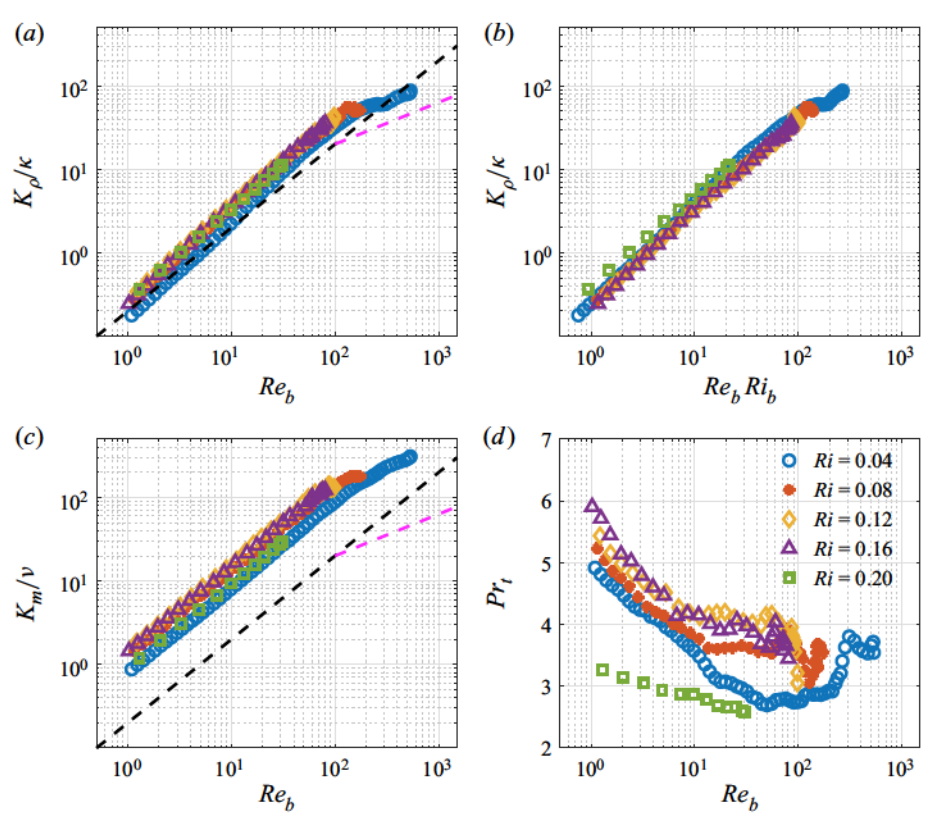


Figure 18. Effect of (a) buoyancy Reynolds number (Re_b) and (b) combined buoyancy Reynolds number and bulk Richardson numbers (Re_b Ri_b) on turbulent diffusivity (K_ρ). Variability of turbulent viscosity (K_m) and turbulent Prandtl number (Pr_t) on Re_b are shown in panels (c) and (d), respectively. The dashed black lines in panels (a,c) indicate the parameterization, $K_\rho/\kappa = K_m/\nu = 0.2Re_b$, from Osborn (1980) with the assumption of $Pr = Pr_t = 1$. The dashed magenta lines in panels (a,c) indicate the parameterization, $K_\rho/\kappa = K_m/\nu = 2Re_b^{1/2}$ for $Re_b > 10^2$, from Shih et al. (2005) with the same assumption of $Pr_t = 1$.

data as $K_{\rho}(t) = \int \varepsilon_{\rho} \, \mathrm{d}z / \int N^2 \, \mathrm{d}z$ where the z-integration is over L_{sl} . Figure 18(a) shows the turbulent diffusivity to exhibit piecewise dependence on Re_b similar to the piecewise dependence of Γ_{3d} on Re_b . Disregarding the decrease of Γ_{3d} in the diffusive regime, K_{ρ} exhibits a linear dependence on Re_b for $Re_b \leq 10^2$ similar to Osborn's model. However, the model underestimates K_{ρ} which suggest a higher constant value of the flux coefficient can improve said model. In the energetic regime $(Re_b > 10^2)$, K_{ρ} is found to be proportional to $Re_b^{1/2}$ similar to the results of Shih *et al.* (2005) although the proportionality coefficient is larger in the present study. It should be noted that Salehipour & Peltier (2015) also found the Re_b -dependence for K_{ρ} in shear layers with a two-layer density profile to be similar to the result in Shih *et al.* (2005), e.g. see their figure 5.

Taking into account the effects of both Re_b and Ri_b , it is found that K_ρ can be parametrized based on the product of Re_b and Ri_b as shown in figure 18(b). The choice of $Re_bRi_b \approx \varepsilon/\nu S^2$ is equivalent to using S as a characteristic inverse time scale rather than N in the mixing parameterization. This parameterization scheme is promising because it prescribes K_ρ over the entire range of Re_b , unlike the piecewise dependence observed when only Re_b is used. It is noted that the bulk parameters in the present study do not

A VanDine, H.T. Pham and S. Sarkar

extend sufficiently into the energetic regime (only the Ri = 0.04 case includes a large range of Re_B) and additional simulations at a higher Reynolds number are required to test whether this parameterization works well for the energetic regime.

We now move to the turbulent viscosity (R_m) and its parameterization. By definition of the turbulent viscosity, it follows that $K_m = P/S^2$, where P is the turbulent production. The equilibrium assumption for the TKE equation is used to write P = e + B and the part of B responsible for irreversible mixing (e_p) is retained so that the turbulent viscosity becomes $K_m = (e + e_p)/S^2$. Abult value of $K_m(t)$ is computed here using bulk (integrals over L_{nl}) values of e_t , e_p and S^2 . Figure 18(c) shows that K_m cannot be described by the Osborn model in this flow. Results from Shith e al. (2005) for homogeneous shear flow indicate that $P_T = 1$ in the intermediate regime and decreases in the energetic regime (where R_B is also low) to $P_T \approx 0.6$. In the present study P_T , exceeds 2.5 in all simulated cases for all mixing regimes. These higher values of P_T are related to the higher R_B in this problem. For example, R_B increases from its initial value of (0.04 to 0.5) during 30 < t < 60 when the flow transitions to turbulence and into the energetic regime. Thus, unlike homogenous shear flow, the energetic regime with large R_B is accompanied by a significant increase of R_B in this flow and, consequently, $P_T = R_B / E_B / E_B$ is alrege ven in the energetic regime. Furthermore, once buoyancy becomes sufficiently strong to bring R_B down to ≈ 10.00 . Pr₁(t) increases with decreasing $R_B/(t)$ because E_M commences a decrease from its peak value.

6. Discussion and conclusions

In the present study DNS of a shear layer with uniform density stratification were performed to investigate turbulence and mixing at a Reynolds number (R_B) of 24000, a high value for DNS. Th

Turbulent shear layers in a uniformly stratified background

Turbulent shear production and an increase in the MKE. Strong stratification tends to inhibit the growth of CGMT and CGBF since they do not occur in the $Ri \geqslant 0.12$ cases. The shear and stratification in the sheared zone evolve to profiles which are different from those found in the canonical two-layer problem. Mashayek et al. (2013) and Salchipour et al. (2016) find that the largest value of the evolving bulk Richardson number $Ri_k(n)$ in the problem with a two-layer density profile is 0.5. Here, $Ri_k(n)$ can reach up to 1.2. Furthermore, multiple layers with differing Ri_g including $Ri_g > 1$ form.

While the rich dynamics of the secondary instabilities in the present case with domain-filling stratification are similar to those for a two-layer density profile, the mixing efficiency in the present study is significantly different. Mashayek et al. (2013) who used a two-layer density profile found a narrow range of Ri with an optimal rate of turbulent mixing, and the cumulative mixing efficiency (E^C based on the mixing over the entire flow evolution) peaks at a value of 0.45 when Ri = 0.16. For the present case of uniform stratification, we find E^C to be considerably smaller (approximately 0.33) in the cases with $Ri \geqslant 0.08$. Also, E^C remains relatively constant among these cases suggesting a much wider range of Ri for optimal turbulent mixing.

A TL with elevated local stratification and shear forms at each edge of the shear layer owing to vertical turbulent fluxes which transport mass and momentum outward from the central region. The two TLs bound a central zone where the shear and stratification profiles are quite different from their initial shape. The central zone takes the form of a layer with some variability of shear and stratification (Ri_0). As Ri_0 increases, the TL becomes thinner. The local N^2 (z) in the TL of the present configuration can be more than twice larger than Ri_0 in contrast to the two-l

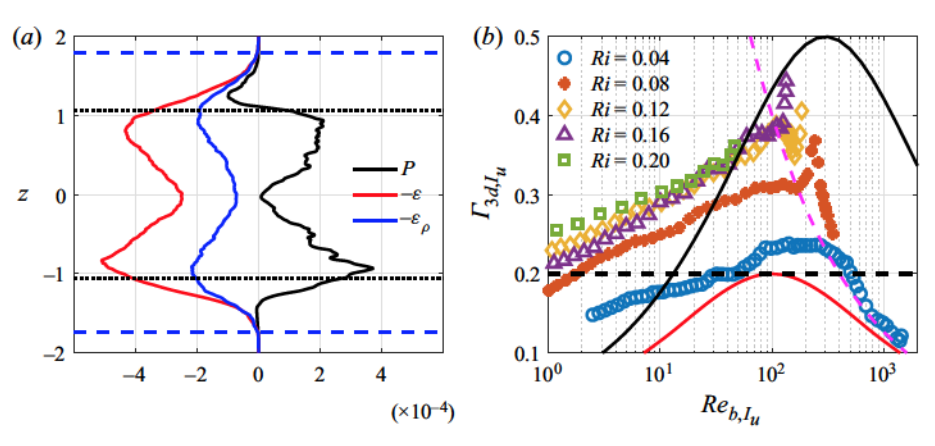


Figure 19. Effect of alternative choices, I_u and L_{sl} , for the length scale of the turbulent zone. (a) Profiles of turbulent production (P), dissipation (ε) and dissipation of the potential energy (ε_ρ) at time t=152 in the Ri=0.12 case. The dotted black lines and dashed blue lines mark the boundaries of the shear layer with $\pm I_u/2$ and L_{sl} , respectively. (b) Dependence of flux coefficient (Γ_{3d,I_u}) on buoyancy Reynolds number (Re_{b,I_u}) when the involved variables are integrated over $\pm I_u/2$ instead of over L_{sl} . The dashed black lines in panel (b) indicate the value of $\Gamma_{3d}=0.2$ suggested by Osborn (1980), while the solid black and red lines denote the upper and lower bounds, respectively, of the Mashayek et al. (2017b) parameterization. The dashed magenta line indicates the parameterization, $\Gamma_{3d}=4Re_b^{-1/2}$ for $Re_b>10^2$ in the Ri=0.04 case also shown in figure 17(b).

monotonically increases, an intermediate regime in which Γ_{3d} remains relatively constant and an energetic regime where $\Gamma_{3d} \sim Re_b^{-1/2}$. When compared with the results of Shih *et al.* (2005), there are some quantitative differences, e.g. the cases with $Ri \geq 0.08$ have higher values of Γ_{3d} . We note that, different from Shih *et al.* (2005), Portwood *et al.* (2019) reported that $\Gamma \propto Re_b^{-1/2}$ dependence does not exist for $100 < Re_b < 1000$ in a recent DNS study with similar set-up. They argue that a transient effect in Shih *et al.* (2005) is the possible cause of the scaling. Our results support the validity of the $\Gamma \propto Re_b^{-1/2}$ scaling. When Γ_{3d} is parametrized as a function of the Froude number (Fr), the flux coefficient in the present study also exhibits similar dependence as observed in the study of homogeneous stratified forced turbulence of Maffioli *et al.* (2016). The peak value of Γ_{3d} occurs at $Fr = \varepsilon/NK \approx 0.2$ and it decreases as Fr deviates from this value.

The results for the mixing-efficiency parameterization depend on the choice employed for the vertical length scale of the shear layer. Figure 19(a) shows that the vertical profiles of turbulent production, TKE dissipation and TPE dissipation extend outside the boundaries of the shear layer marked by $\pm I_u/2$. Clearly, the shear-layer thickness (L_{sl}) is able to include the entire turbulent mixing zone better than I_u . The relationship between the flux coefficient and the buoyancy Reynolds number (figure 19b) using $\pm I_u/2$ has some differences with that obtained using L_{sl} (figure 17b). Comparison of figures 17(b) to 19(b) reveals the agreement with the scaling $\Gamma_{3d}=4Re_b^{-1/2}$ in the energetic regime ($Re_b>10^2$) in the Ri=0.04 case is less when I_u is used as the vertical length scale. The flux coefficient decreases monotonically with decreasing Re_b in the intermediate regime ($40 < Re_b < 100$) while it remains relatively constant when L_{sl} is used as the length scale in the cases with $0.08 \le Ri \le 0.16$. The values of the flux coefficient using $\pm I_u/2$ are considerably smaller in the intermediate regime for all cases since the high-efficiency mixing in the TLs is excluded.

Turbulent shear layers in a uniformly stratified background

Turbulent shear layers in a uniformly stratified background

The mixing efficiency in the cases with $Ri \geqslant 0.08$ exceeds Osborn's model value of 1/6 over the entire turbulent state. Similar to the results of Salehipour et al. (2016), E_{3d} also exhibits a dependence on R_{Ib} . While Salehipour et al. (2016) suggested that the mixing efficiency reaches its peak value of approximately 0.33 when $R_{Ib} = 0.4$ and is saturated when $R_{Ib} = 1.1$, E_{3d} in the $R_I = 0.12$ case reaches its maximum value of 0.31 when R_{Ib} is as large as 1.2. The larger R_{Ib} found in the present study is directly related to the stronger stratification in the TLs. The turbulent diffusivity (K_R) and turbulent viscosity (K_m) are larger than Osborn's model prediction as well as Shih et al. (2005). During entry into the initial energetic regime when R_{Ib} increases to > 100, R_{Ib} also becomes large so that the turbulent Paradid number $(P_T \sim R_B)$ E_{Ib} is larger than in Shih et al. (2005) and (2005) or Salehipour et al. (2016). In the other regimes, P_T , increases with decreasing R_{Ib} similar to other flows. The results of the present study further confirm that turbulent mixing and its parameterization is sensitive to flow conditions including the shape of initial velocity and density profiles. The evolution of R_{Ib} is significantly different between two-layer and constant stratification profiles since local N^2 (2) and N^2 (2) would differently. In order for a mixing parameterization to be generally applicable, future efforts would benefit by going beyond the use of bulk parameters to account for problem-dependent variability of local shear and stratification. It should be noted the parameterization of mixing efficiency E^{C} has been shown to decrease at higher P varies from 7 to 700. The mixing efficiency E^{C} has been shown to decrease at higher P varies from 7 to 700. The mixing efficiency E^{C} has been shown to

- A. VanDine, H.T. Pham and S. Sarkar

 A. VanDine, H.T. Pham and S. Sarkar

 FRITTS, D. 1982 Shear excitation of atmospheric gravity waves. J. Atmos. 5ci. 30, 1936-1952.

 FRITTS, D. 1982 Shear excitation of atmospheric gravity waves. J. Atmos. 5ci. 30, 1936-1952.

 FRITTS, D. 1982 Shear excitation of atmospheric gravity waves. J. Atmos. 5ci. 30, 1936-1952.

 FRITTS, D. 1982 Shear excitation of atmospheric gravity waves. J. Atmos. 5ci. 30, 1936-1952.

 FRITTS, D. 1982 Shear excitation of atmospheric gravity waves. J. Atmos. 5ci. 30, 1936-1952.

 FRITTS, D. 1982 Shear excitation of atmospheric gravity waves. J. Atmos. 5ci. 30, 1936-1952.

 FRITTS, D. 1982 Shear excitation of atmospheric gravity waves. J. Atmos. 5ci. 30, 1936-1952.

 FRITTS, D. 1982 Shear excitation of atmospheric gravity waves. J. Atmos. 5ci. 30, 1936-1952.

 FRITTS, D. 1982 Shear excitation of atmospheric gravity waves. J. Atmospheric gravity and mixing efficiency in the cecan Atmospheric gravity of the stability of the stability of the stability of inviscid stratified athear flows. J. Fluid Meck. 86, 1932-1933.

 HAZIR, P. 1972 Mannerical studies of the stability of inviscid stratified shear flows. J. Fluid Meck. 51, 39-61.

 HOWLAND, C.J., TAYLOK, J.R. & CALLIFIELD, C.P. 2020 Mixing in forced stratified turbulence and its deposition of the stability of inviscid stratified shear flows. J. Fluid Meck. 51, 1930-1936.

 HOWLAND, C.J., TAYLOK, J.R. & CALLIFIELD, C.P. 2020 Mixing in forced stratified turbulence and its deposition of the stability of the stability of inviscid stratification turbulence, but how much mixing? Atmospheric 1930 Reposition of the stability of the stabi

- Turbulent shear layers in a uniformly stratified background

 SALEHHOUR, H., PELTHE, W.R. & MASHAYUK, A. 2015 Turbulent diappean mixing in stratified shear flower the influence of Prandit number on mixing efficiency and transition at high Reynolds number. J. Flaid Mech. 713, 178–223.

 SALEHHOUR, H., PELTHER, W.R. & MASHAYUK, A. 2015 Turbulent diappean inting in stratified shear flower the influence of Prandit number on mixing efficiency and transition at high Reynolds number. J. Flaid Mech. 713, 178–223.

 SALEHHOUR, H., PELTHER, W.R. & WIALEN, C.B. & MACKINNON, J.A. 2016 A new characterization of the turbulent diappeal diffusivities of mass and momentum in the ocean. Geophys. Res. Lett. 43 (7), 3370–3379.

 SCOTTI, A. & WIITT, B. 2014 Diagnossing mixing in stratified turbulent flows with a locally defined available potential energy. J. Fluid Mech. 740, 114–135.

 SHIH, L.H., KOSEFF, J.R., PERZICIER, J.H. 2006 The materization of turbulent fluxes and scales using hornogeneous sheared stably stratified turbulence simulations. J. Fluid Mech. 525, 193–214.

 SMY1G, J.327–1420, J.N. 2000 Length Scales of turbulence in stably stratified mixing layers. Phys. Fluids.

 SMY1H, W.D., MOUM, J.N. & CALDWELL, D.R. 2001 The efficiency of mixing in turbulent patches: inferences from direct simulations and microstracure observations. J. Phys. Geology 31, 1969–1992.

 SMYTH, W.D., MOUM, J.N. & NASH, J.D. 2011 Natrovband oscillations at the upper equatorial ocean. Part III. properties of shear instabilities. J. Phys. Oceanog. 41, 142–1428.

 STRANG, E.J. & FERNANDO, H.J.S. 2001 Entrainment and mixing in stratified shear flows. J. Fluid Mech. 428, 149–386.

 TAKAMURE, K., TIO, Y., SAKAI, Y., IWANO, K. & HAYASE, T. 2018 Momentum transport process in the quasis elf-similar region of free shear mixing layer. Phys. Fluids 30, 015109.

 THORPE, S.A. 2012 On the Keivin-Hollmoltz route to turbulence. J. Fluid Mech. 80, 205–207.

 VANDME, A., CROSSERIENNO, K. & KOSEEP, J.R. 2016 On the flux Richardson number in stably stratified urbulence. J. Flui